

UNCLASSIFIED

AD NUMBER
AD482092
NEW LIMITATION CHANGE
TO Approved for public release, distribution unlimited
FROM Distribution authorized to U.S. Gov't. agencies and their contractors; Administrative/Operational Use; Apr 1966. Other requests shall be referred to US Army Electronics Command, Attn: AMSEL-VL-E, Ft Monmouth, NJ.
AUTHORITY
USAEC ltr, 27 Jul 1971

THIS PAGE IS UNCLASSIFIED

AD



482092

TECHNICAL REPORT ECOM-01253-3

# STUDY OF AIRBORNE MILLIMETER RADAR TECHNIQUES

THIRD QUARTERLY REPORT

BY

L. CHANZIT - L. KOSOWSKY - K. RITTENBERG  
A. HONIG - R. DIDOMIZIO - M. SELVIN - L. STERRITT

APRIL 1966

# ECOM

UNITED STATES ARMY ELECTRONICS COMMAND · FORT MONMOUTH, N.J.

DA28-643 AMC - 01253 (E)

NORDEN DIVISION UNITED AIRCRAFT CORP.

Norwalk, Connecticut

RECEIVED  
MAY 23 1966  
E

**DISTRIBUTION STATEMENT**

This document is subject to special export controls and each transmittal to foreign governments or foreign nationals may be made only with prior approval of CG, U.S. Army Electronics Command, Fort Monmouth, N.J.  
Attn: AMSEL-VL-E

### Disclaimers

The findings in this report are not to be construed as an official Department of the Army position, unless so designated by other authorized documents.

The citation of trade names and names of manufacturers in this report is not to be construed as official Government indorsement or approval of commercial products or services referenced herein.

### Disposition

When this report is no longer needed, Department of the Army organizations will destroy it in accordance with the procedures given in AR 380-5. Navy and Air Force elements will destroy it in accordance with applicable directions. Department of Defense contractors will destroy the report according to the requirement of Section 14 of the Industrial Security Manual for Safeguarding Classified Information. All others will return the report to the controlling DA office.

TECHNICAL REPORT ECOM-01253-3

APRIL 1966

STUDY OF AIRBORNE  
MILLIMETER RADAR  
TECHNIQUES

THIRD QUARTERLY REPORT

1 OCTOBER TO 31 DECEMBER 1965

Report No. 3

CONTRACT NO. DA 28-043 AMC-01253(E)

Prepared By

L. CHANZIT, L. KOSOWSKY, K. RUTTENBERG,  
A. HONIG, R. DIDOMIZIO, M. SELVIN, L. STERRITT  
NORDEN DIVISION UNITED AIRCRAFT CORP.  
NORWALK, CONN.

U. S. ARMY ELECTRONICS COMMAND, FORT MONMOUTH, N.J.

**DISTRIBUTION STATEMENT**

This document is subject to special export controls  
and each transmittal to foreign governments or  
foreign nationals may be made only with prior  
approval of CG, U.S. Army Electronics Command,  
Fort Monmouth, N.J.

Attn: AMSEL-VL-E

## ABSTRACT

Technical progress is reported on the work accomplished during the third quarter of contract No. DA 28-043 AMC-01253(E) entitled, Airborne Millimeter Radar Techniques Study (Obstacle Avoidance) with the United States Army Electronics Command, Fort Monmouth, New Jersey. During the reporting period, work continued on the following principal tasks:

Advanced Sensor Techniques  
Mathematical System Modeling for Computer  
Simulation  
Millimeter Radar Experiments

### Advanced Sensor Techniques

Research into clutter discrimination by means of frequency agility is presented. A model has been developed which exhibits the characteristics of observed clutter. The transmitted frequency has been varied and the electric field reradiated from the model, has been computed. The results indicate a marked dependence of the backscatter signal on the amount of frequency agility. Spectra are presented which indicate energy shift over the clutter band.

The study of signal processing techniques for resolution improvement has continued and preliminary results of an azimuth compression technique are presented. Optical data processing techniques have been investigated for use in identifying obstacles.

### Mathematical System Modeling for Computer Simulation

A digital simulation of an intermediate frequency amplifier has been accomplished which incorporates limiting and bandpass filtering. A simple horn antenna has been simulated which can be used as the building block for more complex aperture illumination functions.

### Millimeter Radar Experiments

The statistical analysis of radar data obtained at Ballistics Research Laboratory, Aberdeen, Maryland, has been completed and the probability density functions are presented. The data has been correlated with the power spectral densities published in ECOM-01253-2.

The millimeter radar has been completed and is described in detail. Initial experiments have indicated that the system is very stable and can be used for reliable clutter and obstacle measurements. Data taken with the radar, at 70 GHz, is published and pertinent characteristics are discussed.

## FOREWORD

This program is being conducted under Contract No. DA 28-043 AMC-01253(E) with the United States Army Electronics Command, Fort Monmouth, New Jersey. The DA Task No. is 1E1-20601-A-219-03-01.

The work described in this third quarterly report represents significant progress toward achieving the goals of this program. Stated briefly, our purpose is to provide a program of study, investigation, and applied research which is intended to supply some of the basic information on which to base the design of future (1975 generation) airborne obstacle avoidance equipment for use in Army aircraft under tactical conditions. To meet these goals, our program is organized under three major technical tasks, namely:

- Task 20 - Physical Characteristics of Obstacles
- Task 30 - Advanced Sensor Techniques
- Task 40 - Mathematical Modeling for Computer Simulation

Detailed descriptions of these tasks are given in Technical Report ECOM-01253-1. The remainder of this section describes the accomplishments of the work performed during this quarter, within the framework of the over-all program goals.

Task 20 has been completed and has been described in detail in report ECOM-01253-1. Significant and useful data have been obtained on:

- a. surface density and height characteristics of vertical obstacles to be found in typical rural, suburban, and small urban areas
- b. attenuation and backscatter cross section characteristics of the atmosphere (including precipitation) at millimeter and optical wavelengths

Task 20 also includes the following items, which are described in report ECOM-01253-2.

- a. an extensive annotated bibliography of references on the scattering characteristics of various types of target shapes
- b. an extensive tabulation of equations for calculating the backscatter cross section of typical target shapes
- c. a study of possible target signatures

Task 30 continues the research into clutter discrimination techniques utilizing frequency agility. In order to evaluate the effects of frequency shifting techniques on the reradiation characteristics of scatterers, a suitable model was sought which displays the observed behavior of true clutter. Such a model has been developed, based on the multiple radiator model of Kerr [1] and Goldstein [2], and is shown to behave as actual clutter. The frequency of transmission is then varied in accordance with a sinusoidal function of time and the signal characteristics are observed. The results show a marked dependence of the backscatter signal on the amount of frequency agility. Spectra are computed which indicate the shift in energy over the band.

Task 30 includes an initial investigation into optical data processing techniques which may be of use in identifying and recognizing obstacles. Such techniques have been developed for high resolution side-looking radar systems and may prove useful in the present study.

The study of signal processing techniques for resolution improvement has continued and the work to date is described. Significant improvements in azimuth resolution may be achievable by the synthetic aperture approach.

Under Task 40, a digital simulation of an intermediate frequency amplifier has been accomplished which incorporates limiting and band-pass filtering. A simple horn antenna has been simulated which can be used as the building block for more complex aperture illuminations and shapes. These programs are being combined with our previously determined clutter programs to develop a complete radar simulation.

The statistical analysis of radar data obtained at the Ballistics Research Laboratory, Aberdeen, Maryland, has been completed and the probability density functions are presented. The data has been correlated with the power spectral densities published in ECOM-01253-2 to furnish a complete statistical picture of several objects measured at 70 GHz.

The millimeter radar has been completed and is described in detail. Initial experiments have indicated that the system is very stable and can be used for reliable clutter and obstacle measurements. Data taken with the radar, at 70 GHz, is published and pertinent characteristics are discussed.

## Table of Contents

<u>Section</u>	<u>Title</u>	<u>Page</u>
1.	TECHNICAL DATA	1
1.1	Physical Characteristics of Obstacles	1
1.2	Advanced Sensor Techniques	1
1.3	Mathematical System Modeling for Computer Simulation	35
1.4	Experimental Millimeter Radar	54
2.	LITERATURE CITED	75
Appendix		
A	DISTRIBUTION LIST	A-1

## LIST OF ILLUSTRATIONS

<u>Figure</u>		<u>Page</u>
1	n-Scatterer Model	3
2	Rayleigh Probability Density Function	4
3	Exponential Probability Density Function	6
4	Magnitude of the Square of the Electric Field Re-radiated by a 10-Scatterer Model	8
5	Power Spectral Density, $W(f)$ , of the n-Scatterer Model, for $n = 10$	9
6	Probability Density of the Signal of Figure 4	10
7	Magnitude of the Square of the Electric Field Re-radiated by a 10-Scatterer Model	11
8	Probability Density of the Signal of Figure 7	12
9	Magnitude of the Square of the Electric Field Re-radiated by a 10-Scatterer Model	13
10	Probability Density of the Signal of Figure 9	14
11	Magnitude of the Square of the Electric Field Re-radiated by a 10-Scatterer Model	15
12	Probability Density of the Signal of Figure 11	16
13	Probability Density Function of Ground Clutter Taken at 9.2 Cm	17
14	Probability Density Function of Ground Clutter Taken at 9.2 Cm	18
15	Sum of 10 Pulses with Linearly Varying Carrier from Pulse to Pulse	26
16	Sum of 10 Pulses of Random Amplitudes, with Linearly Varying Carrier from Pulse to Pulse	27
17	Sum of 10 Pulses with Linearly Varying Carrier of Random Phase from Pulse to Pulse	28
18	Sum of 10 Pulses with Linearly Varying Carrier of Random Phase from Pulse to Pulse	29
19	Sum of 10 Pulses with Linearly Varying Carrier of Random Phase from Pulse to Pulse	30
20	Basic Space Coherent Information Processor [11]	32
21	Basic Space Incoherent Information Processor [11]	34
22	IF Amplifier to Be Simulated	36
23	Steady State Frequency Response of a Two Stage IF Amplifier	38

LIST OF ILLUSTRATIONS (Continued)

<u>Figure</u>		<u>Page</u>
24	Noisy Sinusoidal Input	40
25	Output of First Stage of IF Amplifier	41
26	Output of Second Stage of IF Amplifier	42
27	Radiation Coordinate System	43
28	Spherical Coordinates	45
29	Aperture Partitioning and Excitation	46
30	H-Plane Field Intensity Pattern	47
31	H-Plane Field Intensity Pattern	48
32	Voltage H-Plane Pattern for a Cosine Excitation	50
33	H-Plane Antenna Pattern	51
34	E-Plane Antenna Pattern	52
35	E-Plane Antenna Pattern	53
36	Experimental Millimeter Radar	55
37	60 ns Pulse, Transmitted at a Peak Power of 900 Watts	58
38	Return from a Tree with No Foliage	58
39	Clutter Spectrum from Trees at 1000 Feet in Range	59
40	Return from an Aluminum Cable	60
41	Return from a Tree with No Foliage	60
42	Return from the Metal Gutters on a Wooden House	62
43	Return from a Telephone Pole	62
44	Radar Spectrum of Return from Chimney at 2.9 Miles in Range	63
45	20 ns Pulse	64
46	Return from the Metal Gutters on a Wooden House	64
47	Block Diagram of the System Used to Obtain Estimates	66
48	Results of a Test Run	67
49	Probability Density Function of Radar Echo	68
50	Probability Density Function of Radar Echo	68
51	Probability Density Function of Radar Echo from Reference Sphere	69
52	Probability Density Function of Radar Echo from Isolated Telephone Pole	70
53	Probability Density Function of Radar Echo from Vertically Suspended cable	71
54	Probability Density Function of Radar Echo from Telephone Pole	72

## 1. TECHNICAL DATA

### 1.1 Physical Characteristics of Obstacles

Task 20 has been completed. Reference should be made to reports ECOM-01253-1 and ECOM-01253-2 for the results of this investigation.

### 1.2 Advanced Sensor Techniques

Research into clutter discrimination by means of frequency agility is presented. A model has been developed which exhibits the characteristics of observed clutter. The transmitted frequency has been varied and the electric field reradiated from the model has been computed. The results indicate a marked dependence of the backscatter signal on the amount of frequency agility. Spectra are presented which indicate energy shift over the clutter band.

Optical data processing techniques have been investigated for use in identifying obstacles. Further research into this area will be made in the next reporting period. The study of signal processing techniques for resolution improvement has continued and preliminary results of an azimuth compression technique are presented.

#### 1.2.1 Clutter Discrimination By Means of Frequency Agility

##### 1.2.1.1 Introduction

In order to evaluate the effects of frequency shifting techniques on the reradiation characteristics of scatterers, a suitable model was sought which displays the observed behavior of true clutter. Such a model has been developed based on the multiple radiator model of Kerr [1] and Goldstein [2] and is shown to behave as true clutter. The frequency of transmission is then varied in accordance with a sinusoidal function of time and the signal characteristics are observed. The results show a marked dependence of the backscatter signal on the amount of frequency agility. Spectra are computed which indicate the shift in energy over the band.

##### 1.2.1.2 The Scatterer Model

The development of a model to obtain the desired power spectrum characteristics was achieved through the use of a group

of randomly moving scatterers. As shown in Figure 1, "n" scatterers are arranged such that their mean positions are uniformly distributed in range. Each scatterer is permitted to move at an arbitrary velocity and to have an arbitrary starting position. The resulting time function observed at the receiver is the vector sum of the electric field from each of the scatterers. In the sections which follow, the results of such a model will be examined and compared with predicted clutter characteristics.

### 1.2.1.3 Clutter Characteristics

The signal radiated by a large group of scatterers has been studied on a statistical basis for many years. The theoretical models which have served to describe observed phenomena generally consist of an infinite number of independent scatterers, each free to move at a different velocity. The description of the total signal emanating from such an array forms a branch of the general theory of random processes dating back to Rayleigh [3].

The total received electric field strength can be shown to be of the form [4]:

$$E(t) = R(t) \cos[\omega_0 t + \phi(t)] \quad (1)$$

where  $\omega_0$  is the transmitted frequency and  $R(t)$  and  $\phi(t)$  are functions of scatterer motion. If we define a vector  $\vec{R}(t)$ , whose magnitude is equal to  $R$  and whose phase is  $\phi$ , then the probability density function of  $R$ , i.e., the probability that  $R$  lies between  $R$  and  $R + dR$ , is given by the well known Rayleigh distribution [5]:

$$p\left(\frac{R}{\sqrt{P_0}}\right) = 2\left(\frac{R}{\sqrt{P_0}}\right) e^{-\left(\frac{R}{\sqrt{P_0}}\right)^2} \quad (2)$$

A plot of equation (2) is given in Figure 2. The mean value of  $\frac{R}{\sqrt{P_0}}$  is  $\frac{\sqrt{\pi}}{2}$  and the rms value is  $\frac{1}{2} \sqrt{(4-\pi)}$ .

If we consider the signal energy,  $P$ , which is proportional to  $R^2$ , then the probability density function of  $P$  is given as [5]:

$$g\left(\frac{P}{P_0}\right) = e^{-\frac{P}{P_0}} \quad (3)$$

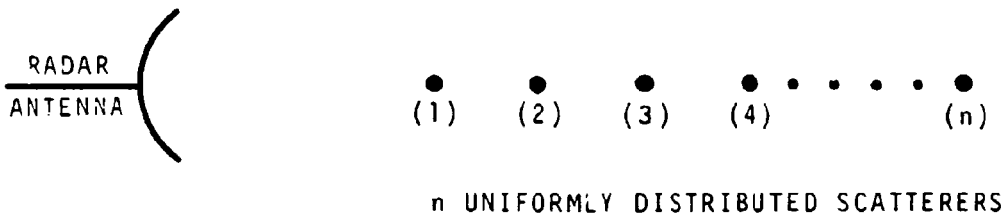


Figure 1. n-Scatterer Model

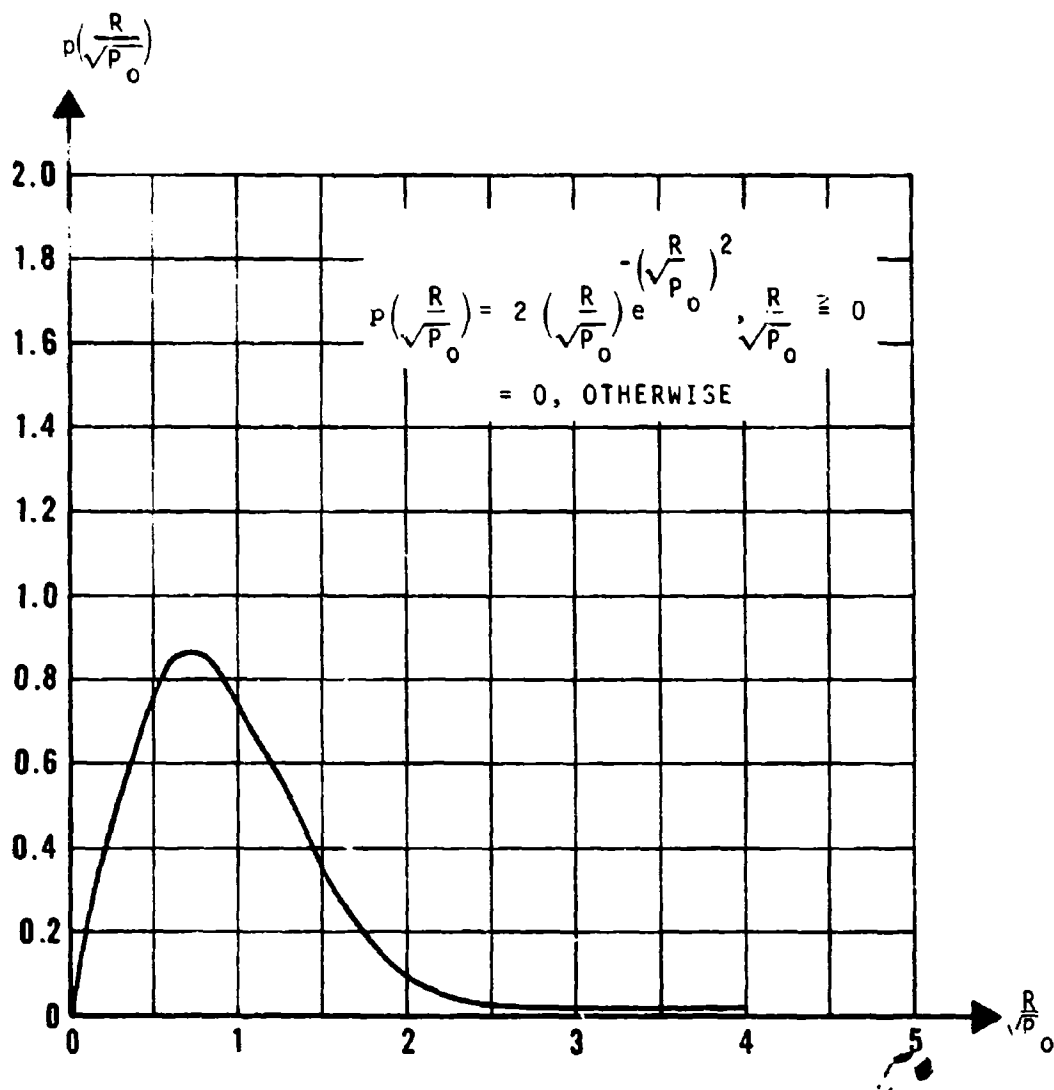


Figure 2. Rayleigh Probability Density Function

A plot of equation (3) is shown in Figure 3.

Extending the discussion to the case of a fixed target return plus clutter, Schwartz [6] has shown that,

$$p(R) = \frac{2Re}{P_0} \exp\left(-\left(\frac{R^2}{P_0} + m^2\right)\right) I_0(2mR/\sqrt{P_0}) \quad (4)$$

where  $I_0$  is the modified Bessel function, and  $m^2$  is the signal-to-noise power ratio. For  $m^2 \gg 1$ , equation (4), reduces to the Gaussian function:

$$p(R) = \frac{1}{\sqrt{\pi P_0}} e^{-\left(\frac{R}{\sqrt{P_0}} - m\right)^2} \quad (5)$$

Thus, for high signal-to-noise ratios, the power spectral density rapidly approaches a Gaussian distribution with mean  $m\sqrt{P_0}$  and standard deviation  $\sqrt{P_0}/2$ .

Up to this point we have been concerned with the long-term statistics of clutter which essentially determine the averages [6] of the noise process. Now let us examine the correlation between samples of the clutter signal spaced at  $\tau$  second intervals, i.e., the autocorrelation function of the clutter process. This problem has not been solved analytically for the model discussed previously although much experimental data has been obtained for a wide variety of scatterer mobilities and forcing functions, such as wind. The Fourier transform of the autocorrelation function is the power spectral density and it is with this function that we shall be concerned. Barlow [7] suggests that a good approximation to the experimentally determined spectral density, valid over a wide range of radar frequencies, is given by:

$$W(f) = e^{-a\left(\frac{f}{f_0}\right)^2} \quad (6)$$

where "a" is a spectrum parameter dependent on the composition of the area being observed and  $f_0$  is the frequency of operation.

In terms of these two quantities, namely the probability density function and the power spectral density, we can now discuss the random scatterer model.

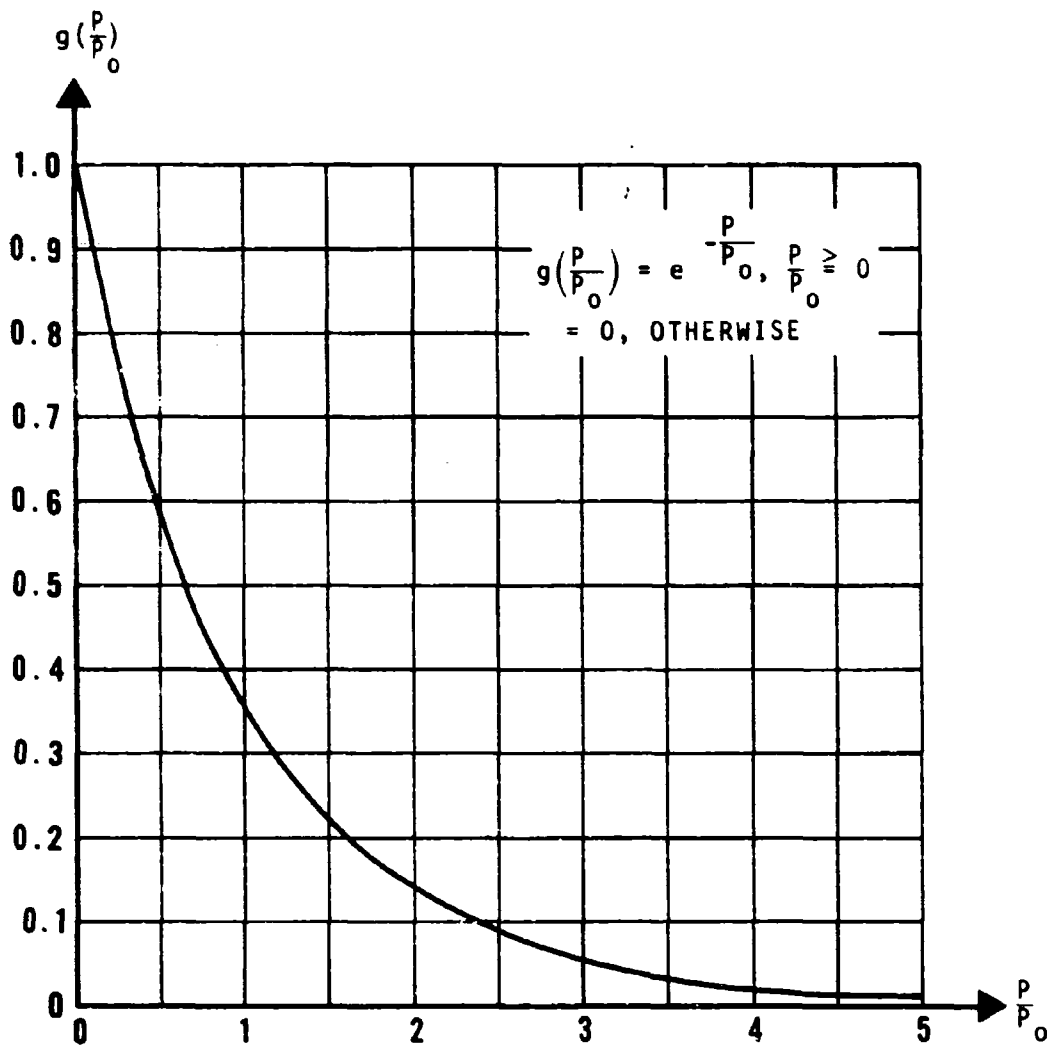


Figure 3. Exponential Probability Density Function

#### 1.2.1.4 Experimental (Computer) Results

The scatterer model discussed in Section 1.2.1.2 was programmed for  $n=10$  and has been run at both 16.5 GHz and 70 GHz without frequency agility. The resultant time function is shown in Figure 4.<sup>(1)</sup> Detailed analyses of the nature of the time function were made to determine its reliability as a realistic clutter simulator.

Figure 5 shows the power spectral density of the model while Figure 6 shows the probability density function of the model, both taken at 16.5 GHz. It is seen that the statistics closely resemble those obtained by Barlow and others [7] for actual terrain. In addition, since the velocity of the scatterers is arbitrary, any width spectrum can be obtained merely by scaling the time base or conversely, the frequency base.

Figures 7, 9, and 11 show the resulting time functions when frequency agility is applied to the model. The statistics of these functions are plotted in Figures 8, 10 and 12.

The similarity between the signal statistics from the model and those obtained experimentally is quite good if reference is made to Kerr [8]. Figures 13 and 14 show the measured probability densities of wooded terrain taken at 10 and 25 mph wind velocities. It should be noted that the probability density goes from exponential to Rayleigh as the wind velocity increases. Comparison between these curves and Figures 6 and 10 shows that frequency agility on the present model produces the same effect as increased wind velocity. It can be seen that an abrupt change in clutter power, or standard deviation, occurs as the magnitude of the frequency shift increases beyond 4 MHz. In addition, pockets of energy appear around harmonics of the shift frequency. A close examination of the time waveform indicates that the high frequency energy is a result of intense interference and occurs infrequently even with frequency agility. The results of these experiments indicate that very large amounts of frequency agility achieve little in whitening the clutter spectrum beyond a certain point. This critical frequency is quite abrupt and will be examined closely in subsequent studies. In addition, slowly moving objects will be placed in the clutter and their characteristics examined for possible signatures.

---

<sup>1</sup> Experimental data at 70 GHz will be presented in the final report.

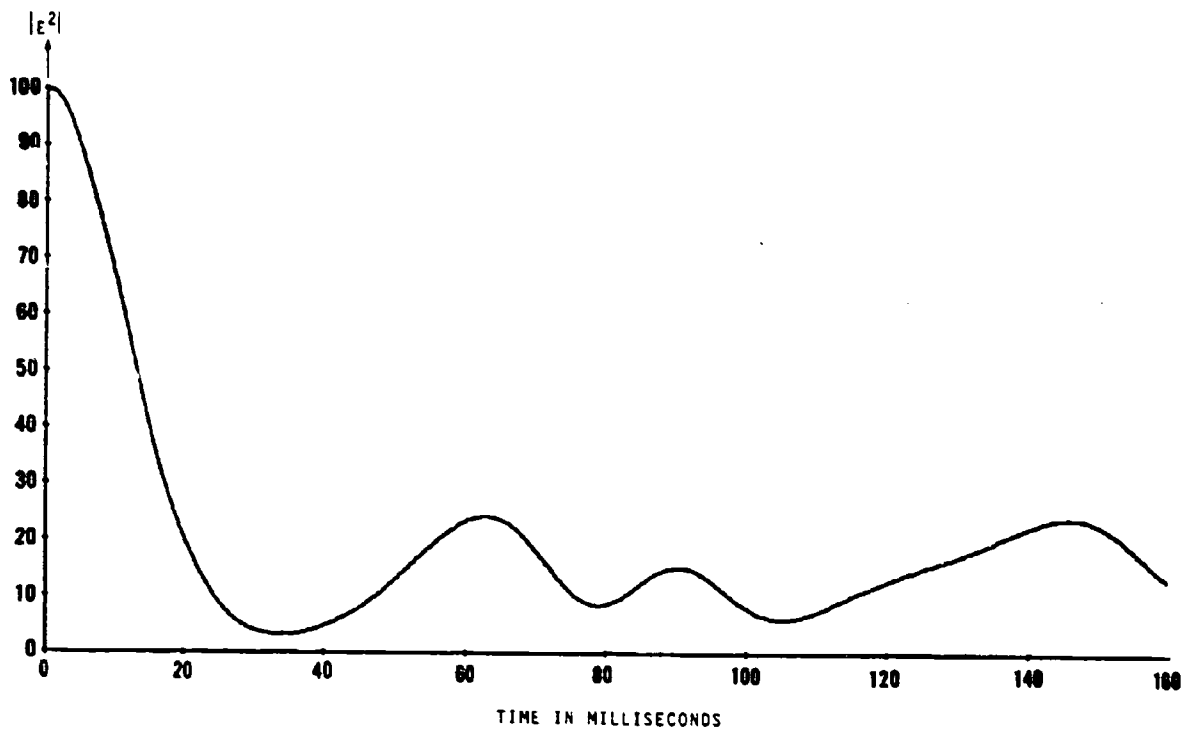


Figure 4. Magnitude of the Square of the Electric Field Reradiated by a 10-Scatterer Model. Frequency of Operation,  $f$ , is 16.5 GHz with a Pulse Repetition Frequency, PRF, of 2400 Hz and Zero Frequency Agility. The Separation between Scatterers is 20 Feet.

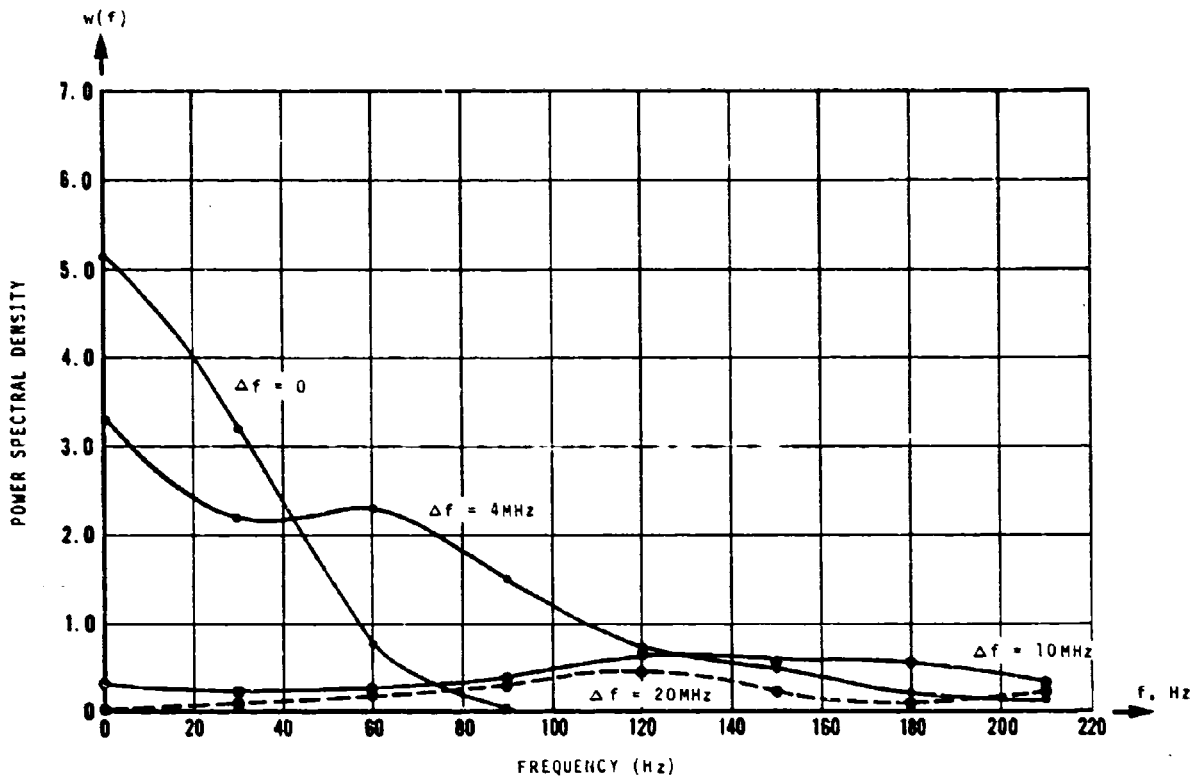


Figure 5. Power Spectral Density,  $W(f)$ , of the  $n$ -Scatterer Model, for  $n = 10$ .  $\Delta f$  is the magnitude of frequency shift.

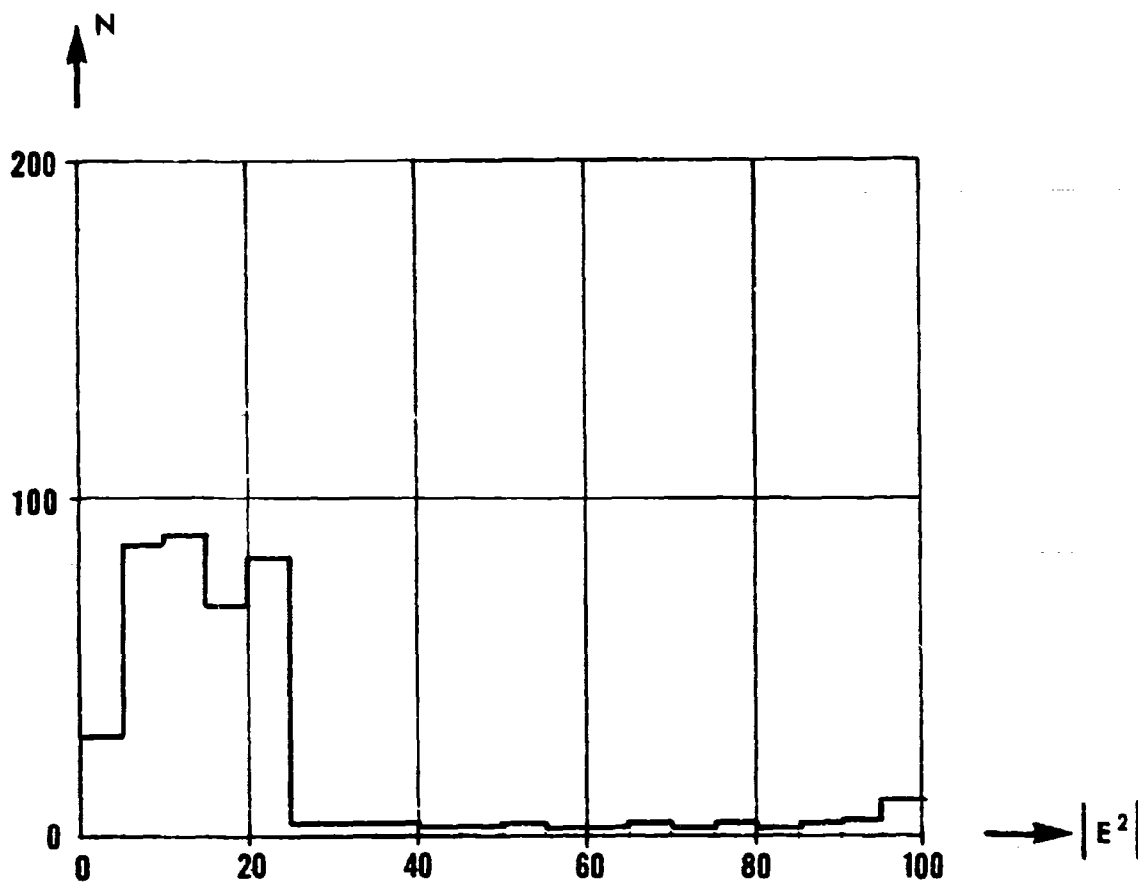


Figure 6. Probability Density of the Signal of Figure 4. N is the Number of Samples Recorded.

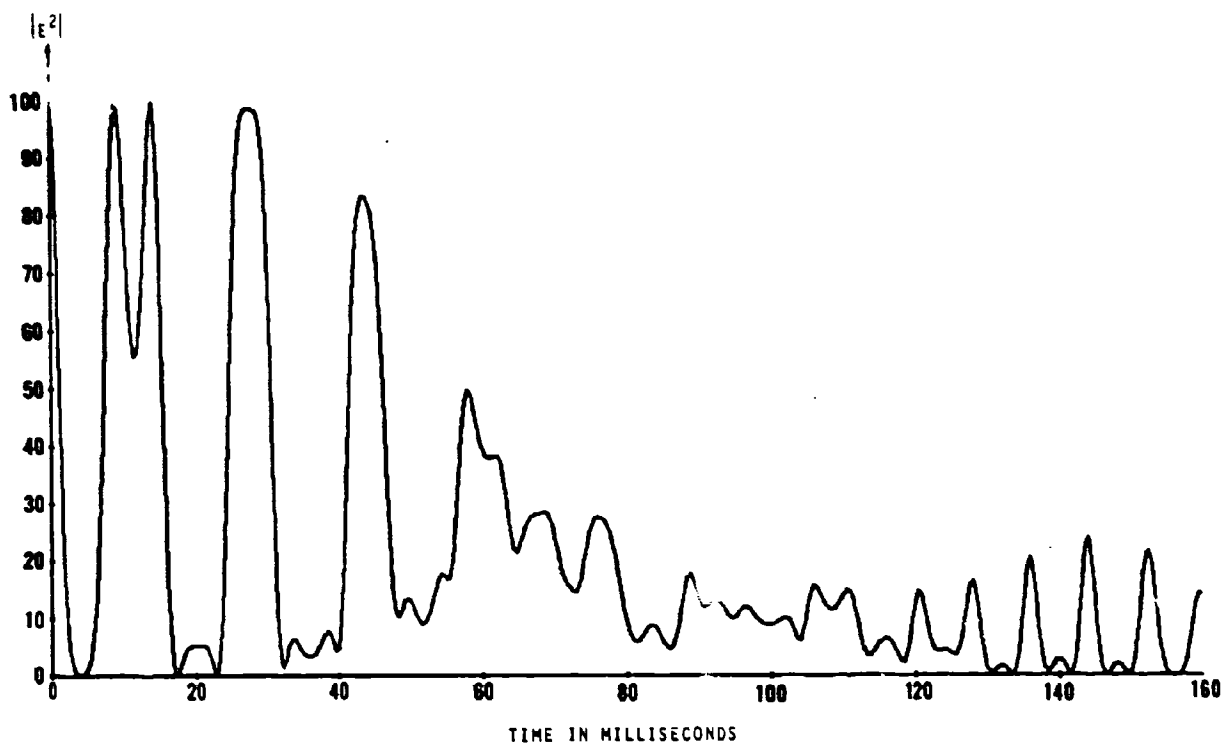


Figure 7. Magnitude of the Square of the Electric Field Reradiated by a 10-Scatterer Model. Frequency of Operation is 16.5 GHz with a Pulse Repetition Frequency, PRF, of 2400 Hz. Frequency Agility with a Magnitude of 4 MHz and a Slew Rate of 60 Hz was Employed. The Separation between Scatterers is 20 Feet.

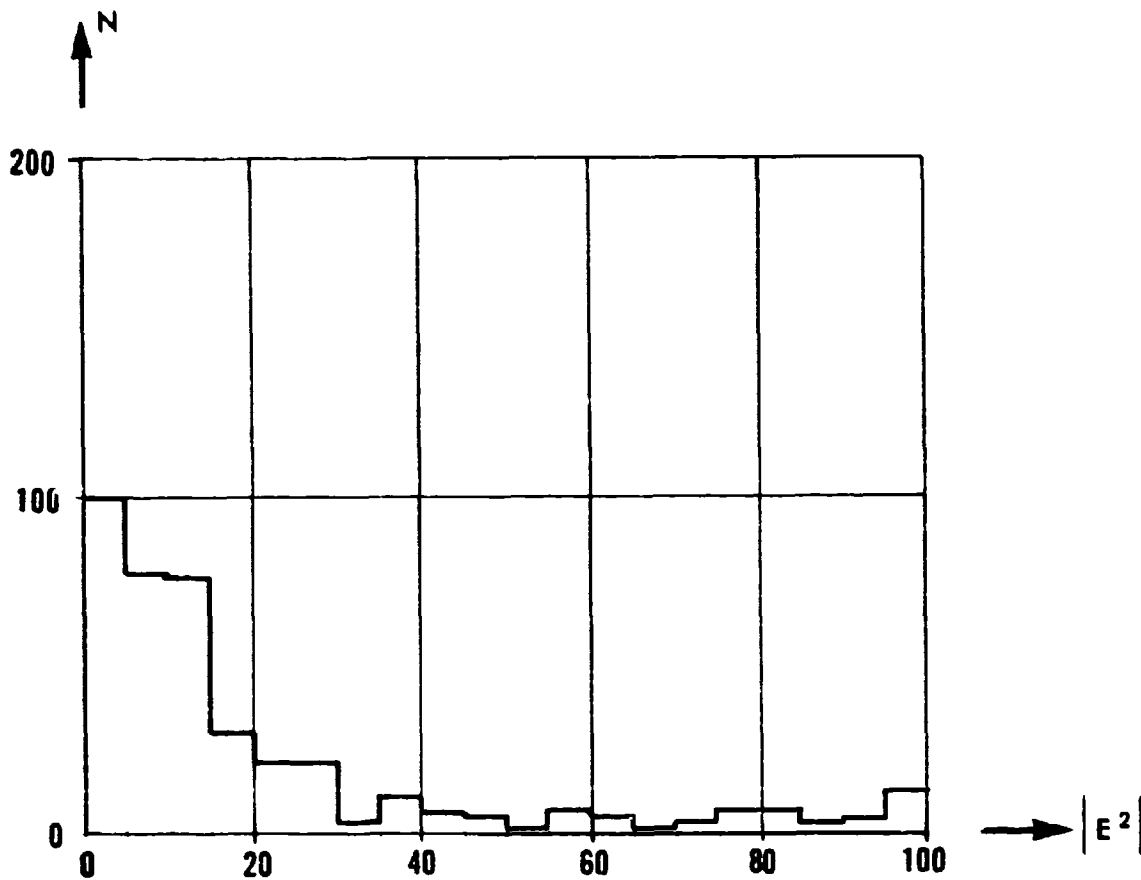


Figure 8. Probability Density of the Signal of Figure 7. N is the Number of Samples Recorded.

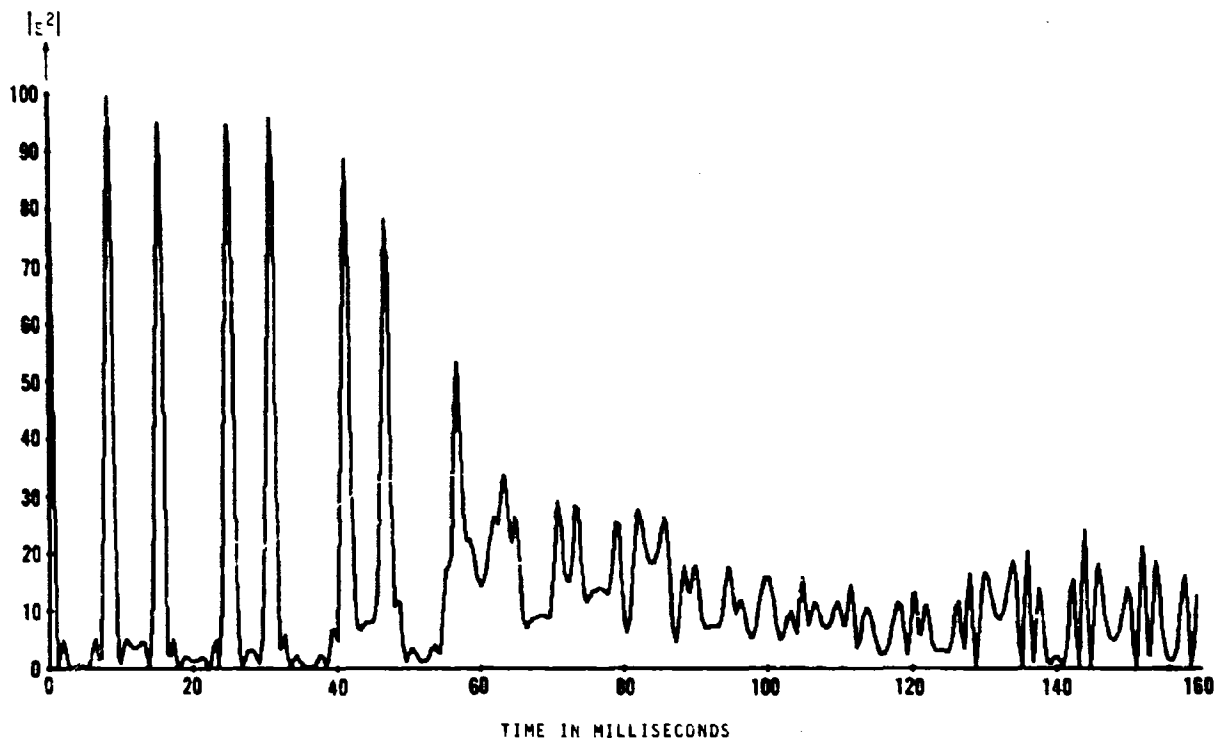


Figure 9. Magnitude of the Square of the Electric Field Reradiated by a 10-Scatterer Model. Frequency of Operation is 16.5 GHz with a Pulse Repetition Frequency, PRF, of 2400 Hz. Frequency Agility with a Magnitude of 10 MHz and a Slew Rate of 60 Hz was Employed. The Separation between Scatterers is 20 Feet.

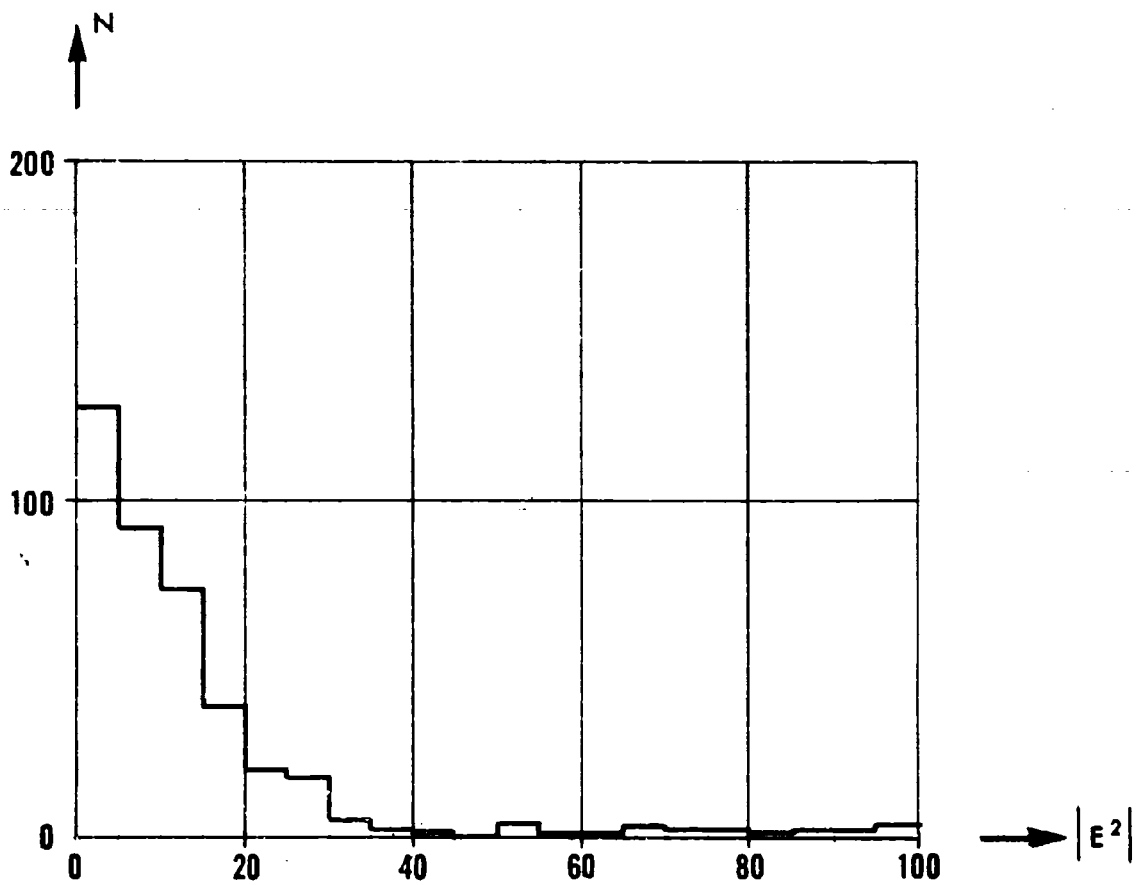


Figure 10. Probability Density of the Signal of Figure 9. N is the Number of Samples Recorded.

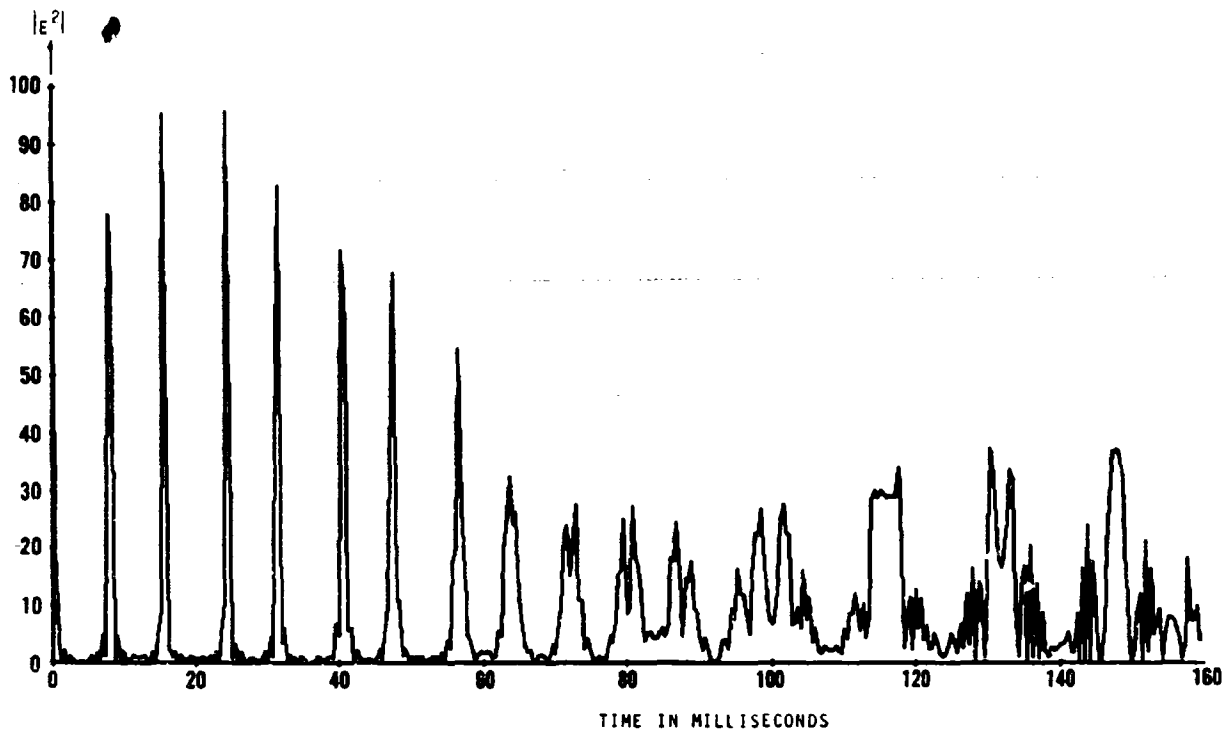


Figure 11. Magnitude of the Square of the Electric Field Reradiated by a 10-Scatterer Model. Frequency of Operation is 16.5 GHz with a Pulse Repetition Frequency, PRF, of 2400 Hz. Frequency Agility with a Magnitude of 20 MHz and a Slew Rate of 60 Hz was Employed. The Separation between Scatterers is 20 Feet.

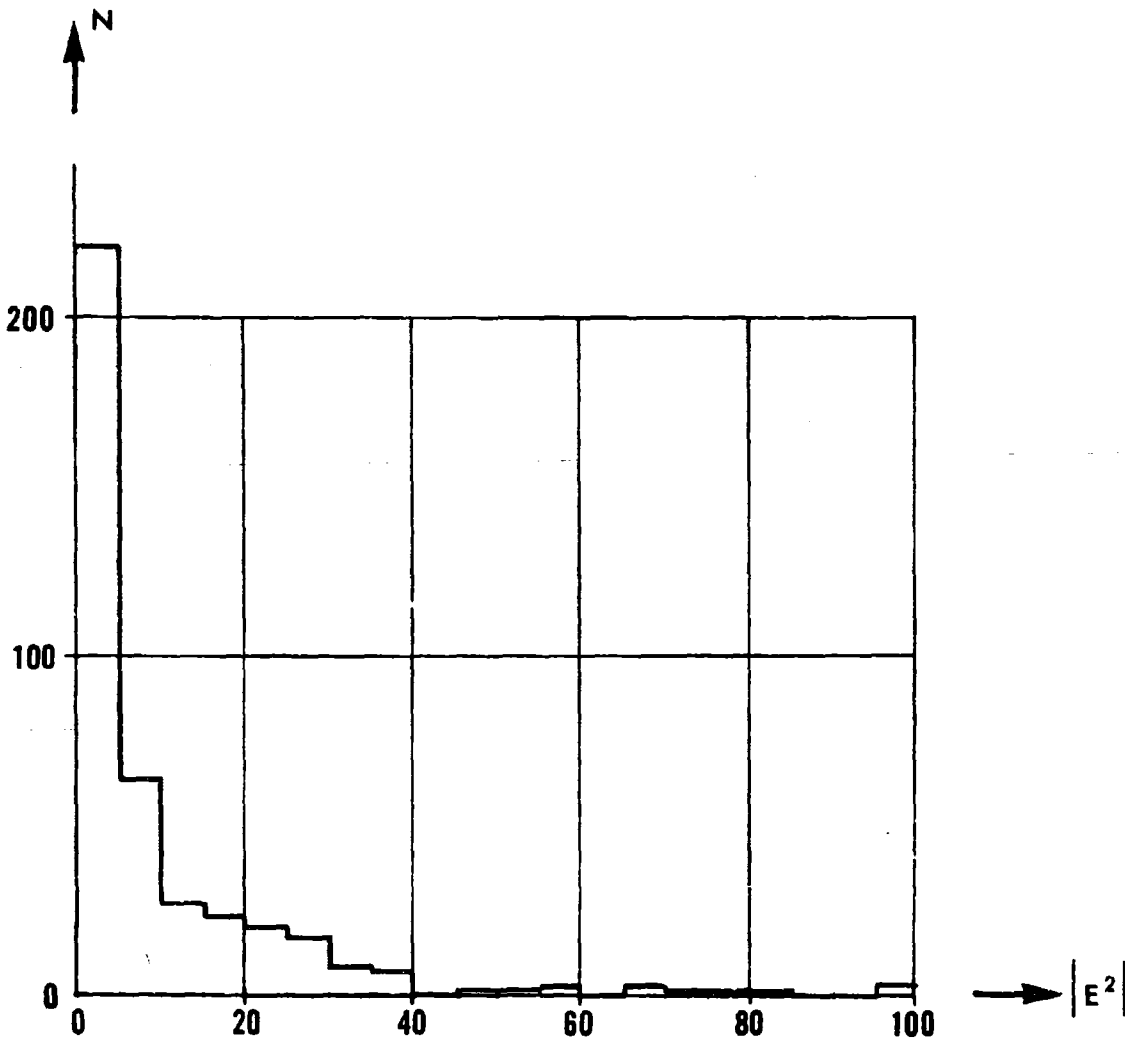


Figure 12. Probability Density of the Signal of Figure 11. N is the Number of Samples Recorded.

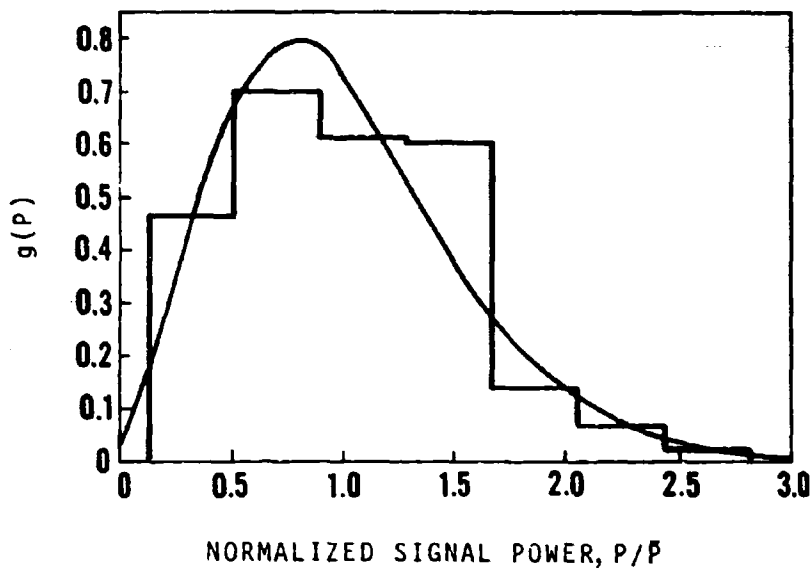


Figure 13. Probability Density Function of Ground Clutter Taken at 9.2 Cm. Heavily Wooded Terrain, Wind Speed 10 MPH.  $\bar{P}$  is the average power. [8]

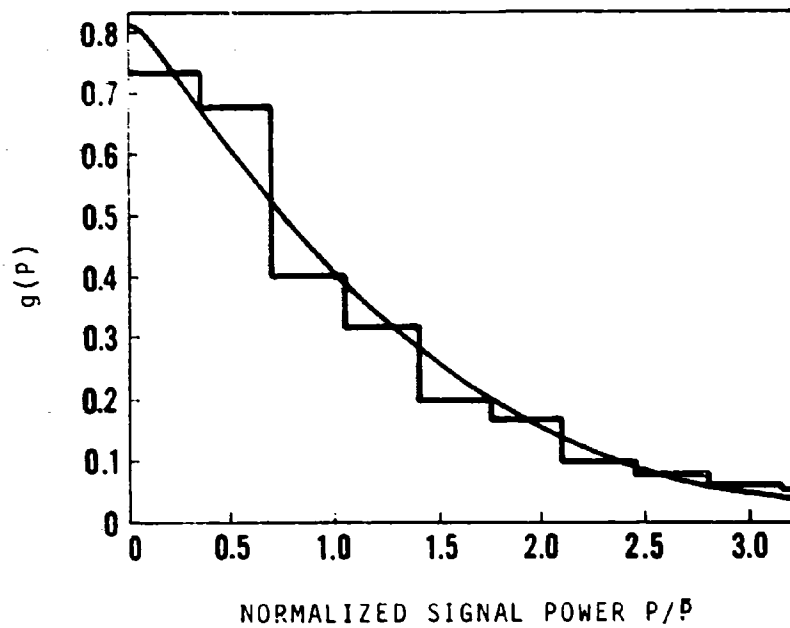


Figure 14. Probability Density Function of Ground Clutter Taken at 9.2 Cm. Heavily Wooded Terrain, Wind Speed 25 MPH.  $\bar{P}$  is the average power. [8]

## 1.2.2 Resolution Improvement By Means of Signal Processing

### 1.2.2.1 Introduction

High resolution in both range and azimuth angle can be achieved simultaneously by means of signal processing techniques. High resolution is achieved utilizing existing low resolution equipment, by the addition of a frequency modulation capability to the transmitter and an appropriate signal processing capability to the receiver. Although a long pulse and a wide azimuth beam are used, the range resolution of a short pulse and the azimuth angle resolution of a narrow azimuth beam are realized.

An azimuth compression technique is used analogous to the commonly employed pulse compression techniques. Frequency modulation is introduced under the azimuth space pattern. The carrier frequency of each individual pulse is kept constant, but the carrier frequency is varied from pulse to pulse. By means of suitable processing, a compressed azimuth space pattern is realized.

Pulse compression techniques commonly transmit a pulse envelope with a linearly increasing carrier frequency. The received pulse is applied to a filter that has a delay characteristic which is a linearly decreasing function of frequency. Thus, the lowest frequency which is received first is delayed the longest, and the highest frequency which is received last, is delayed the least, resulting in a compressed pulse.

An analogous technique is employed in this report for compression in azimuth. Varying the carrier frequency from pulse to pulse introduces frequency modulation within the azimuth space pattern envelope in a manner analogous to the introduction of frequency modulation within a pulse envelope. The series of pulses of different carrier frequency are applied to a filter, with delay varying with frequency. The filter delays each pulse the appropriate amount so that the pulses are all added at the same time, resulting in a compressed azimuth space pattern.

However, there are important differences between using a pulse with modulated carrier for range compression and using a group of pulses with varying carriers for azimuth compression.

A pulse with a linearly modulated carrier, as it travels out in range, illuminates, in turn, each of two point targets separated in range. The returns from both targets are pulses with carriers linearly increasing in an identical manner. However, the two targets do not return the same frequency at

any given time, even though they are separated by less than a pulse width. Thus, each frequency is returned from the two targets at a different time, and one compression filter is sufficient to separate the returns. Since the compression process is a linear one, the output consists of two compressed pulses.

The situation is quite different for a series of pulses with varying carriers. As the antenna scans in azimuth, a target may pass into the beam at any time. Although the return from a target consists of a series of pulses with one complete cycle of the carrier variation<sup>(2)</sup>, the sequence in which the carrier frequencies are returned depends upon where in the cycle the return begins. Thus, the return from a target is a series of pulses which are frequency coded; the code being the sequence in which the carrier frequencies are returned.

One compression filter, matched to that particular sequence, is required for each sequence. The filter for each sequence has an output only when it receives the correct sequence. The filter delays each pulse of the sequence an appropriate amount and then adds them at the correct time.

When two point targets are in the azimuth beam, they both return the same frequency. Two point targets will only return differing sequences if they are separated in azimuth by at least the angle that the antenna moves in the time between pulses. This is the azimuth resolution limit of this technique.

The summation of all the pulses of a sequence at the same time also achieves pulse compression. The summation is that of a number of pulses with varying carriers. For a linear variation, the result is a compressed pulse of width equal to the reciprocal product of the number of pulses and the frequency variation from pulse to pulse.

High azimuth resolution may also be achieved by doppler techniques. However, a fundamental shortcoming of the doppler method is that resolution is a function of the angular position of the targets. This high resolution technique fails for targets on or near dead ahead. The technique of varying the carrier frequency from pulse to pulse does not have this shortcoming.

---

<sup>2</sup> This simple case is used for purposes of illustration. Modifications are necessary in a practical situation.

Section 1.2.2.2 gives an explanation of the mathematical foundation upon which the range-azimuth compression technique is based. Section 1.2.2.3 gives an explanation of how high range and azimuth angle resolution are realized, in particular, by means of a varying carrier from pulse to pulse, based upon the mathematical foundation of section 1.2.2.2.

### 1.2.2.2 Combined Range-Azimuth Angle Ambiguity Function

In order to be able to resolve two targets, the signals returned from the two targets must be separated on the basis of their differences. It can be shown that a measure of the differences between the signals returned from two targets, one at range  $\tau_1$ , (range given in terms of the time delay of return,  $\tau$ ), and azimuth angle  $\theta_1$ , the other at range  $\tau_2$  and azimuth angle  $\theta_2$  is the combined range-azimuth angle ambiguity function given by [9]

$$J_{\tau, \nu}(\tau, \nu) = J_{\tau}(\tau) J_{\nu}(\omega_0 \nu) \quad (7)$$

where  $J_{\tau, \nu}(\tau, \nu)$  = combined range-azimuth angle ambiguity function

$J_{\tau}(\tau)$  = range ambiguity function = autocorrelation function of pulse =  $\int a(t) a^*(t-\tau) dt$ , where (8) star denotes complex conjugate.

$J_{\nu}(\omega_0 \nu)$  = azimuth angle ambiguity function = autocorrelation function of azimuth space pattern =  $\int G^*(\omega_0 \mu) G[\omega_0(\mu + \nu)] d\mu$  (9)

$s(t)$  = returned signal<sup>(3)</sup>  
 $= a(t) e^{j\omega_0 t}$

$a(t)$  = shape of pulse

$\omega_0$  = carrier frequency

$\tau$  =  $\tau_2 - \tau_1$

$G(\omega_0 \mu)$  = azimuth space pattern as a function of angle  
 $\mu = \frac{\sin \theta_1}{c}$

$\mu + \nu = \frac{\sin \theta_2}{c}$

<sup>3</sup> A signal  $s(t)$  may be represented in complex notation as

$$s(t) = \alpha(t) e^{j[\omega_0 t - \phi(t)]} = a(t) e^{j\omega_0 t}$$

where  $a(t) = \alpha(t) e^{j\phi(t)}$

It can be seen from equation (7) that the combined range-azimuth angle ambiguity function is separable into the range ambiguity function and the azimuth angle ambiguity function. Thus, range resolution and azimuth resolution are independent of one another.

The range ambiguity function is the autocorrelation function of the pulse and the azimuth angle ambiguity function is the autocorrelation function of the azimuth space pattern. The range resolution properties are given by the shape of the pulse autocorrelation function and the azimuth angle resolution properties by the shape of the azimuth space pattern autocorrelation function. High resolution is achieved if signals with suitable autocorrelation functions can be found. It will be shown in section 1.2.2.3 that the signal, with carrier varying from pulse to pulse, has an autocorrelation function that gives both azimuth space pattern compression and pulse compression.

The output of a filter matched to a signal <sup>(4)</sup> is the autocorrelation function of that signal as a function of time. The output of each filter matched to a sequence of pulses is the autocorrelation function of the sequence to which it is matched.

#### 1.2.2.3 Compression in Range and Azimuth by Means of Frequency Coding from Pulse to Pulse

Based upon the mathematical foundation of section 1.2.2.2, an explanation is given of range and azimuth angle compression by means of frequency coding.

---

<sup>4</sup> If  $s(t)$  is a time function whose Fourier Transform  $S(\omega) = a(\omega)e^{jB(\omega)}$ , the response of a filter,  $h(t)$ , matched to this signal is given by

$$h(t) = s^*(-t), \text{ where } * \text{ denotes complex conjugate}$$

$$H(\omega) = S^*(\omega) = a(\omega)e^{-jB(\omega)}$$

The output of the matched filter,  $e(t)$ , is given by

$$e(t) = \frac{1}{2\pi j} \int S(\omega)S^*(\omega)e^{j\omega t}d\omega = \frac{1}{2\pi j} \int a^2(\omega)e^{j\omega t}d\omega$$

By adding all the frequency components in phase, the matched filter produces a compressed pulse at its output.

### 1.2.2.3.1 Azimuth Compression

The azimuth space pattern <sup>(5)</sup> is converted to a function of time at the receiver by means of antenna rotation to give

$$G[\omega_0 \dot{u}(t-y)] \quad (10)$$

where

$\omega_0$  = carrier frequency

$\dot{u}$  = antenna scan rate

$y$  = time at which target passes into beam

A typical sequence of pulses returned from a target, with carriers varying linearly from pulse-to-pulse, is given by <sup>(6, 7)</sup>

$$s_p(t) = \sum_{n=m}^{N-1+m} g(\omega_0 \dot{u}t) e^{j[\omega_0 + (n-m)\omega_1][t - (n-m)T - \tau_t]} \text{rect}\left(\frac{t - (n-m)T - \tau_t}{\tau_p}\right) \quad (11)$$

where  $s_p(t)$  = sequence of pulses,  $n = 1, 2, 3, \dots$

$m$  = pulse at which sequence begins

$T$  =  $1/\text{PRF}$

$\tau_p$  = pulse width

$\tau_t$  = delay of target in range

$\omega_1$  = carrier change from pulse-to-pulse

$$\text{rect}(z) = 1, \quad 0 \leq z \leq 1 \\ = 0, \quad z > 1$$

- 
- 5 The effect of the variation of carrier frequency from pulse-to-pulse on the azimuth space pattern is neglected, since the variation is small compared to the original carrier.
  - 6 The phase of the azimuth space pattern is neglected.  $g(\omega_0 \dot{u}t)$  represents the amplitude of the azimuth space pattern as a function of time.
  - 7 For purposes of illustration, it is assumed that the carrier is linearly varied and that the return from a point target contains only one cycle of the carrier variation.

The azimuth space pattern is considered constant during a pulse time giving

$$s_p(t) = \sum_{n=m}^{N-1+m} g[\omega_0 \dot{\nu}(n-m)T] \text{rect} \left( \frac{t - (n-m)T - \tau_t}{\tau_p} \right) e^{j[\omega_0 + (n-m)\omega_1][t - (n-m)T - \tau_t]} \quad (12)$$

The pulses of the sequence are delayed appropriately and then summed at the same time by the filter matched to that sequence. The output of the matched filter,  $m(t)$ , is given by:

$$m(t) = e^{j\omega_0 t'} \sum_{n=m}^{N-1+m} g[\omega_0 \dot{\nu}(n-m)T] \text{rect} \left( \frac{t'}{\tau_p} \right) e^{j[(n-m)\omega_1]t'} \quad (13)$$

where

$$t' = t - (n-m)T - \tau_t$$

#### 1.2.2.3.2 Range Compression

If the pulses are all of equal amplitude, the filter output given by equation (13) becomes:

$$\begin{aligned} m'(t) &= e^{j\omega_0 t'} \sum_{n=m}^{N-1+m} e^{j[(n-m)\omega_1]t'} \text{rect} \left( \frac{t'}{\tau_p} \right) \quad (14) \\ &= e^{j[\omega_0 + (N-1)\omega_1]t'} \frac{\sin \frac{N}{2} \omega_1 t'}{\sin \frac{\omega_1}{2} t'} \text{rect} \left( \frac{t'}{\tau_p} \right) \end{aligned}$$

Equation (14) is a frequency shifted carrier with envelope

$$\frac{\sin \frac{N}{2} \omega_1 t'}{\sin \frac{\omega_1}{2} t'} \text{rect} \left( \frac{t'}{\tau_p} \right) \quad (15)$$

Equation (15) is a compressed pulse of height  $N$  and width  $\frac{1}{N\omega_1}$ . Thus, pulse compression is realized. The results for  $N=10$ ,  $\tau_p = .2 \mu\text{sec}$ ,  $f=4\text{MHz}$ ,  $f_0=100\text{MHz}$  are given in Figure 15.

#### 1.2.2.3.3 Autocorrelation Function

It can be shown that equation (13) is the center term of the autocorrelation function (the other terms are eliminated by the filtering process) of a train of rectangular pulses with carriers varying linearly from pulse to pulse [10]. Thus a filter with this output is a close approximation to a matched filter for that particular frequency-coded sequence.

#### 1.2.2.3.4 Unequal Amplitudes and Random Phases From Pulse to Pulse

Equation (13) is the sum of  $N$  terms of a Fourier series. Equation (14) gives the form of the sum when all the terms have equal amplitudes and equal phases. It is desired to determine the form of the sum when the amplitudes and the phases vary from term to term.

If the terms have unequal amplitudes, but equal phases, the summation is that of  $N$  terms of a Fourier series with real coefficients. The terms all add in phase. The coefficients are given by the azimuth space pattern sampled at regular intervals. If the amplitudes are not greatly different from one another, the envelope is still of the form of equation (15) given by:

$$k \frac{\sin \frac{N}{2} \omega_1 t'}{\sin \frac{\omega_1}{2} t'} \quad (16)$$

However,  $k$  is smaller than 1. An example is given in Figure 16 which is identical to Figure 15, except that the pulses have random amplitudes. However, if the amplitudes of certain components predominate, these determine the shape of the envelope.

The form of the sum when the phases vary determines the degree of coherence required in the system. If the terms have equal amplitudes, but the phases vary, the summation is that of  $N$  terms of a Fourier series with imaginary coefficients. In the worst case, with the phases varying in a random manner, the terms do not add in phase and the form of the envelope of equation (16) is not retained. Figures 17, 18, and 19 show the summation of terms of random phases. The random phases of Figure 17 are multiplied by  $45^\circ$  and  $90^\circ$ , respectively, to obtain the phases of Figures 18 and 19. Appreciable degradation of the envelope does not appear until the values of the random phases approach  $45^\circ$ .

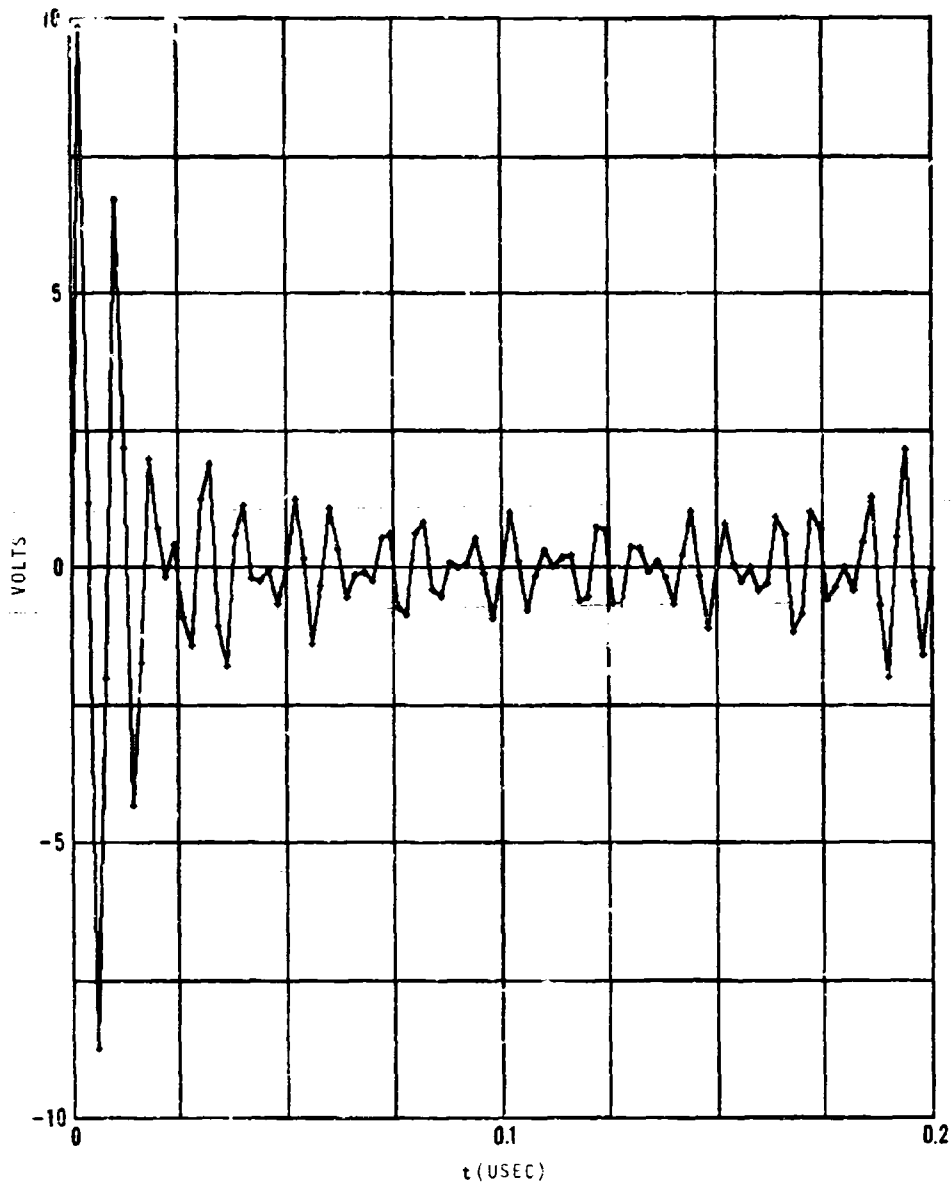


Figure 15. Sum of 10 Pulses with Linearly Varying Carrier from Pulse to Pulse. The Sum

$$\sum_{n=0}^9 \sin [2\pi(f_0 + nf_1)t]$$

is Evaluated with

$$f_0 = 100 \text{ MHz}, f_1 = 4\text{MHz and } \tau_p = 0.2 \text{ } \mu\text{s}.$$

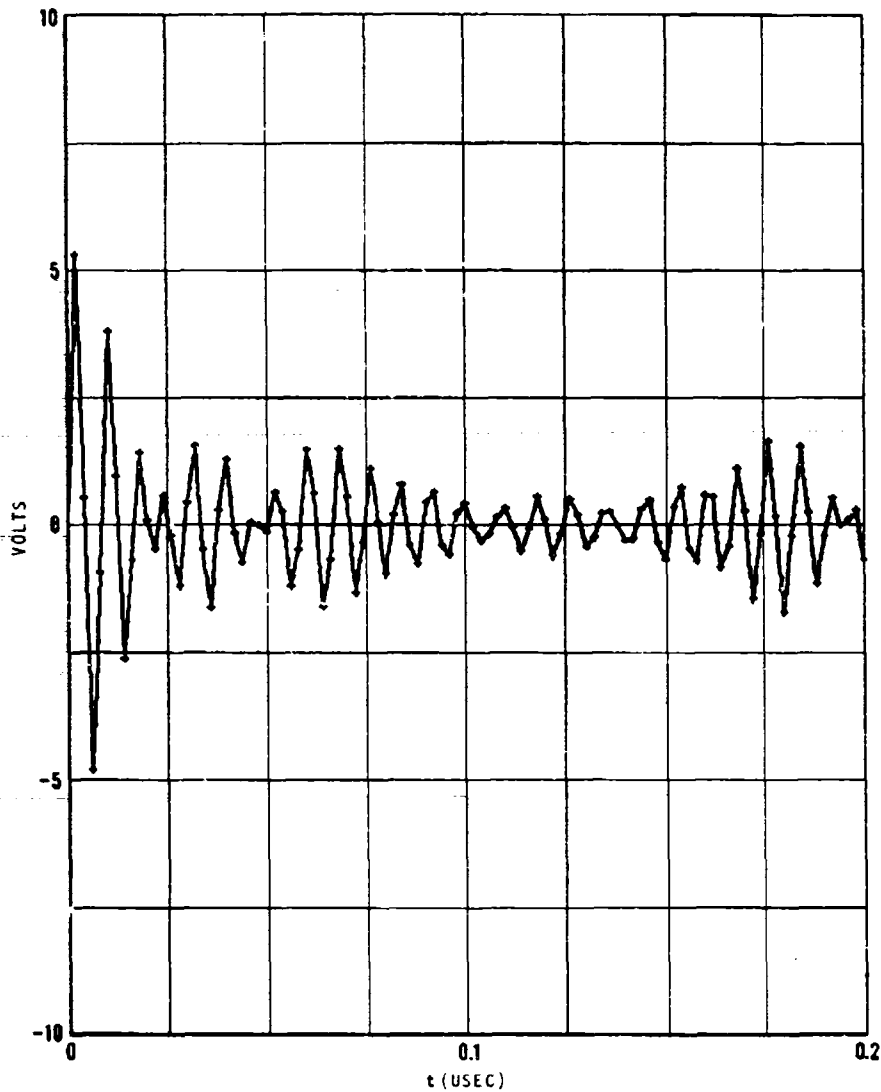


Figure 16. Sum of 10 Pulses of Random Amplitudes, with Linearly Varying Carrier from Pulse to Pulse. The Sum

$$\sum_{n=0}^9 a_n \sin [2\pi(f_0 + nf_1)t] \text{ is Evaluated}$$

with  $f_0 = 100 \text{ MHz}$ ,  $f_1 = 4 \text{ MHz}$  and  $\tau_p = 0.2 \text{ } \mu\text{s}$ .

Amplitudes ( $a_0, a_1, \dots, a_9$ ) are Given by

(0.3, 0.7, 0.5, 0.4, 0.2, 0.8, 0.5, 0.3, 0.9, 0.8).

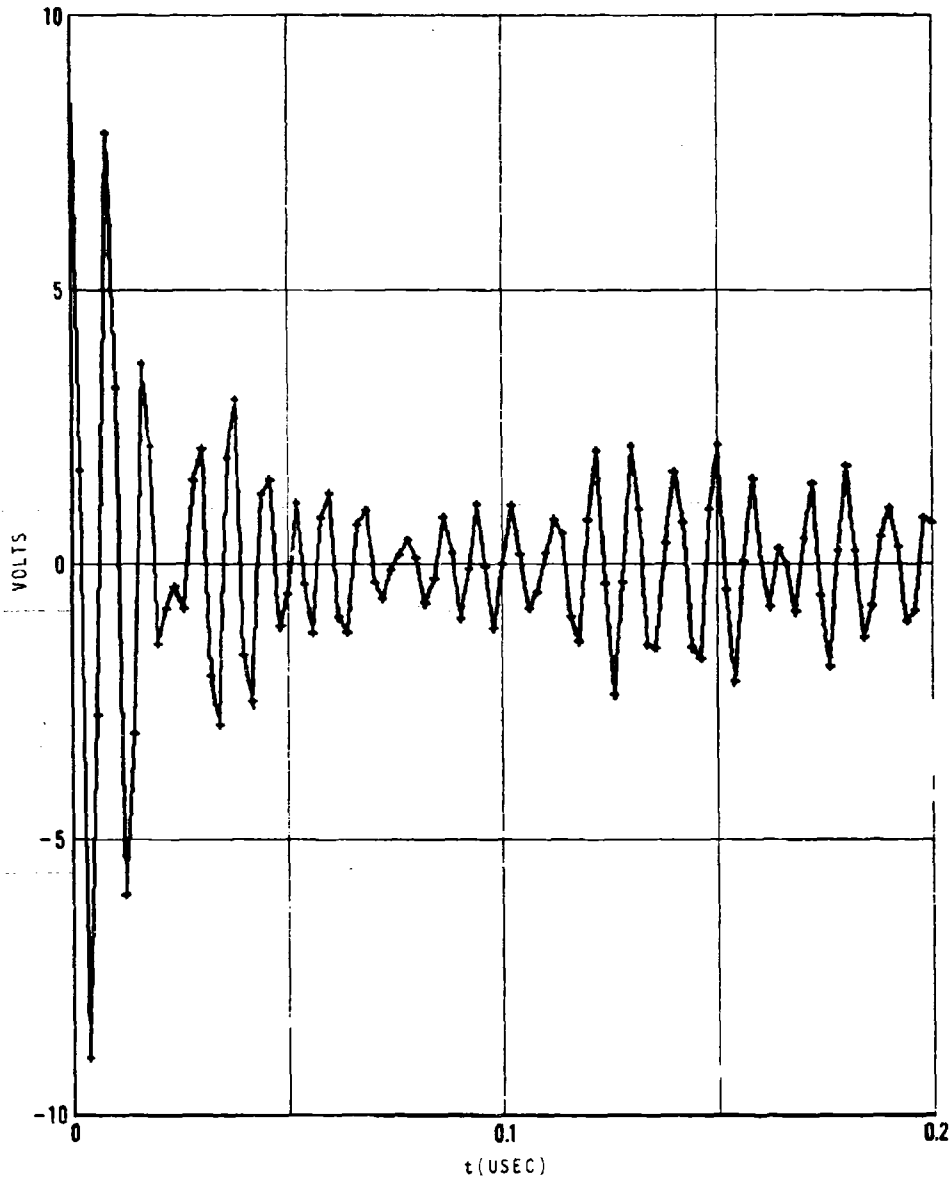


Figure 17. Sum of 10 Pulses with Linearly Varying Carrier of Random Phase from Pulse to Pulse. The Random Phases  $\phi_n$  are Less Than  $1^\circ$ . The

$$\text{Sum}_{n=0}^9 \cos [2\pi(f_0 + nf_1)t + \phi_n] \text{ is Evaluated}$$

with  $f_0 = 100 \text{ MHz}$ ,  $f_1 = 4 \text{ MHz}$  and  $\tau_p = 0.2 \text{ } \mu\text{s}$ .

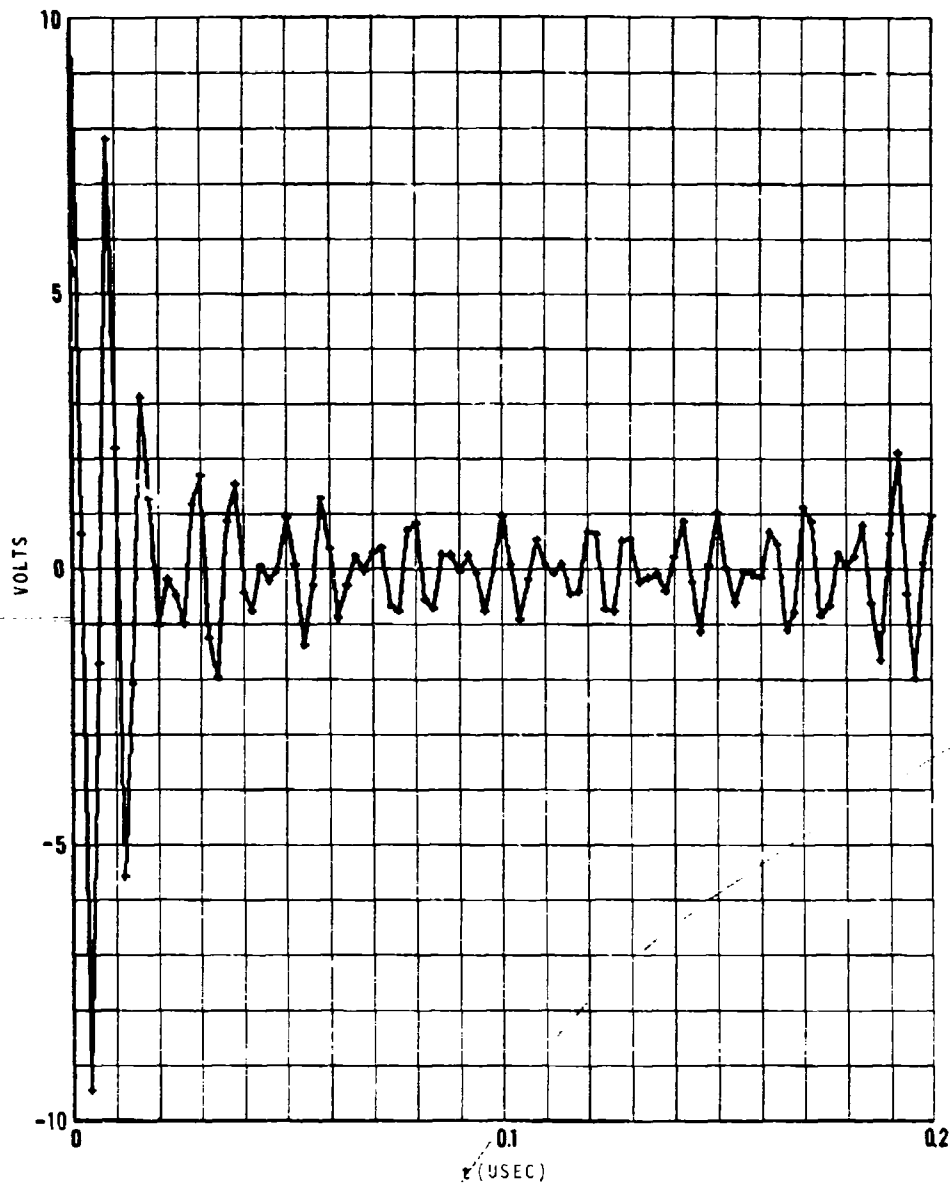


Figure 18. Sum of 10 Pulses with Linearly Varying Carrier of Random Phase from Pulse to Pulse. The Random Phases  $\phi_n$  are Less than  $45^\circ$ .

The Sum

$$\sum_{n=0}^9 \cos [2\pi(f_0 + nf_1)t + \phi_n] \text{ is}$$

Evaluated with  $f_0 = 100 \text{ MHz}$ ,  $f_1 = 4 \text{ MHz}$   
and  $\tau_p = 0.2 \text{ } \mu\text{s}$ .

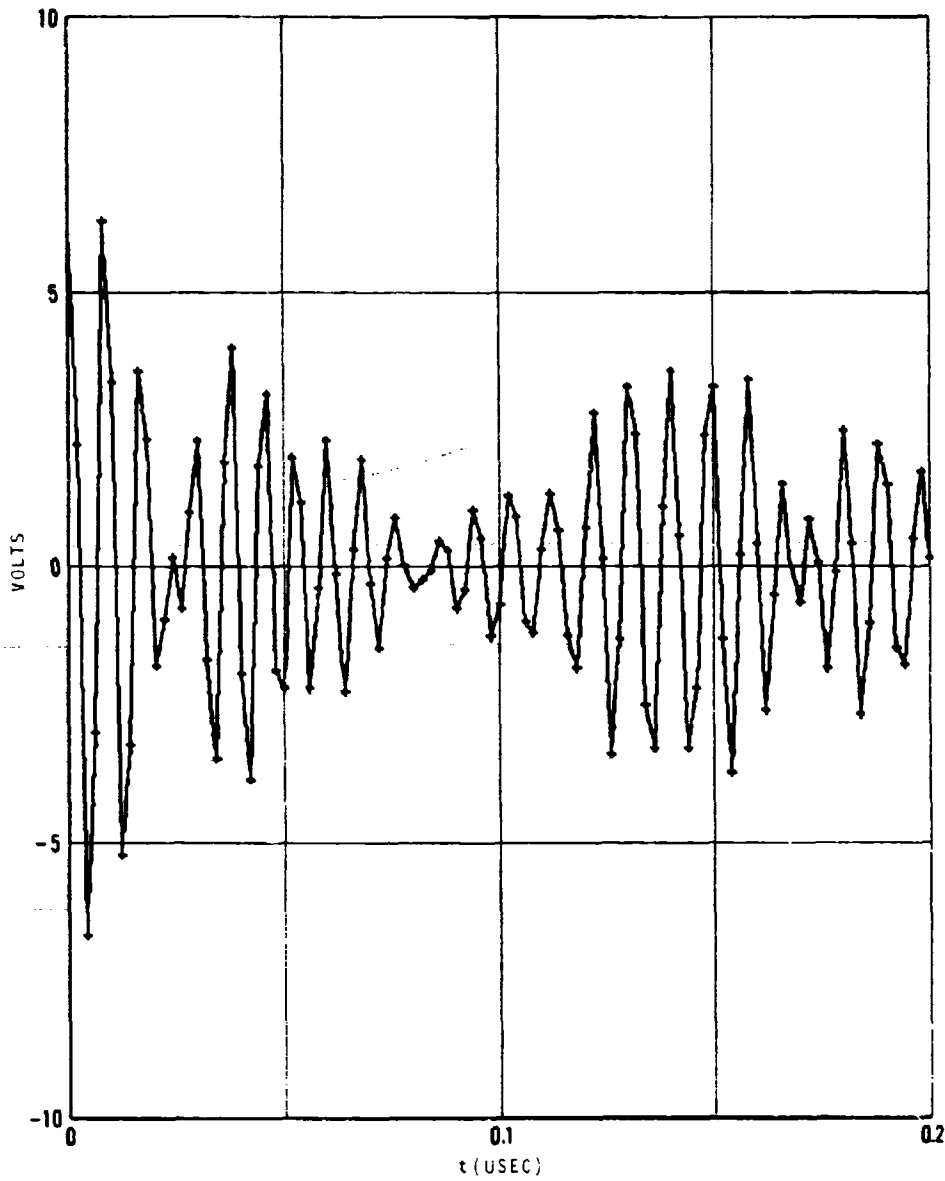


Figure 19. Sum of 10 Pulses with Linearly Varying Carrier of Random Phase from Pulse to Pulse. The Random Phases  $\phi_n$  are Less than  $90^\circ$ .  
The Sum

$$\sum_{n=0}^9 \cos [2\pi(f_0 + nf_1)t + \phi_n] \text{ is}$$

Evaluated with  $f_0 = 100 \text{ MHz}$ ,  $f_1 = 4 \text{ MHz}$   
and  $\tau_p = 0.2 \text{ } \mu\text{s}$ .

### 1.2.3 Electro-Optical Information Processing

The high data rate required for low-altitude obstacle avoidance necessitates a close examination of data processing and display techniques which can handle large amounts in real time. In this section we consider the basic principles of electro-optical data processing which is playing an increasing role in high resolution three-dimensional sensors and displays. The theory underlying optical processing has been studied for a number of years and is being examined for its ability to process large amounts of information for use in obstacle avoidance applications.

#### 1.2.3.1 Introduction

Because certain useful filtering operations may be carried out with greater facility by optical means than by electronic means, the application of electro-optical techniques to the processing of information in a radar system appears to offer certain advantages. One of the primary advantages of optical information processing systems is the high information handling capability resulting from two-dimensional processing as opposed to the one-dimensional processing possible in an electronic circuit. In addition, large quantities of information may be processed efficiently because one process may be simultaneously applied to many signals. Similarly, several processes may be simultaneously applied to the same signal. This results in reduction of system size and complexity.

#### 1.2.3.2 Optical Data Processing

Two general groups of optical data processing are of interest, coherent and incoherent. In both groups, input-output relationships analogous to electronic processors can be obtained.

The first group, the coherent processors, operates on the signal to form its Fourier transform optically. This Fourier transform, which is actually a diffraction pattern, can then be operated upon by spatial techniques. Thus, the coherent processors are equivalent to electronic filters and consequently any linear data processing operation can be performed in a coherent optical processor.

The basic space-coherent processor, shown in Figure 20, consists of two lenses with their optical axes and focal points coincident, illuminated by a space-coherent light source such as a laser. (Since only spatial coherence is required, a monochromatic pin-hole source and suitable collimating equipment could be used.) The light source impinges upon the "signal" which is located at the object plane of the first lens. This signal can be a photographic transparency, or in the case of real time systems such as radar, an ultrasonic light modulator.

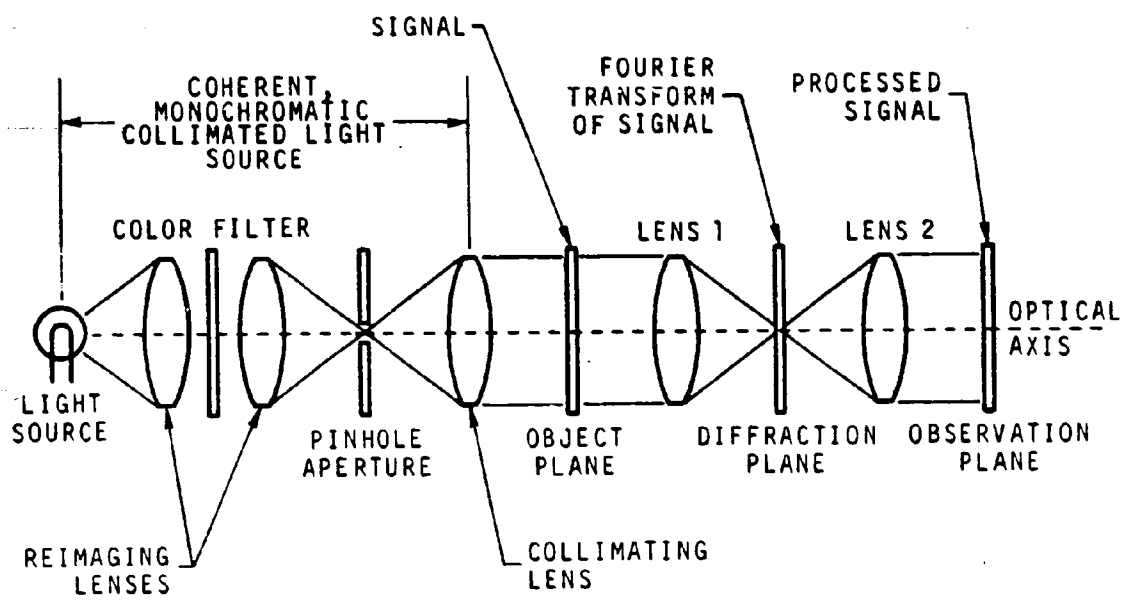


Figure 20. Basic Space Coherent Information Processor [11]

An ultrasonic wave passing through the modulator causes small variations in the index of refraction of the material. As a result, the phase of the entrant plane wave of light will be retarded in some portions of the modulator and advanced in others. The plane wave then emerges as a modulated wavefront. It is expected that these modulators will eventually be fabricated with frequency responses of several gigahertz. The first lens then forms the diffraction pattern of the signal in the diffraction plane between the two lenses. The light amplitude and phase of the diffraction pattern are the Fourier transform of the signal in the object plane. If the amplitude function is then squared (analogous to an electrical power spectrum), the light intensity as a function of position is obtained.

Processing of the signal is accomplished by simple spatial filtering (masking) of the diffraction pattern. The light then passes through the second lens which performs another transform and the processed information is displayed in the observation plane of the second lens.

The second group of optical processors, the incoherent processors, have a somewhat more simple configuration than the coherent processors. A basic incoherent processor, shown in Figure 21, consists of a large diffuse light source, two signal sources (or a signal and a reference source) and a lens, arranged in that order, with their axes coincident. The signal sources, which define two object planes for the lens, can be ultrasonic light modulators or simply photographic transparencies. As rays of light leave the diffuse source at some angle,  $\theta$ , with the optic axis, they pass through the first modulator (object plane 1), and this light acquires the distribution of the first signal  $f_1(x,y)$ . The rays then pass through the second modulator (object plane 2) and the distribution of the light is  $f_1(x,y) \cdot f_2(x + x_0, y + y_0)$ , where  $f_2(x,y)$  is the second signal and  $x_0$  and  $y_0$  are functions of  $\theta$ . The lens then integrates this light and, in the observation plane of the lens, the distribution is given by:

$$\int_{-Y}^Y \int_{-X}^X f_1(x,y) f_2(x+x_0, y+y_0) dx dy \quad (17)$$

This is seen to be a two dimensional analog of the finite time cross-correlation function [11]:

$$\int_{-T}^T f_1(t) f_2(t+\tau) dt \quad (18)$$

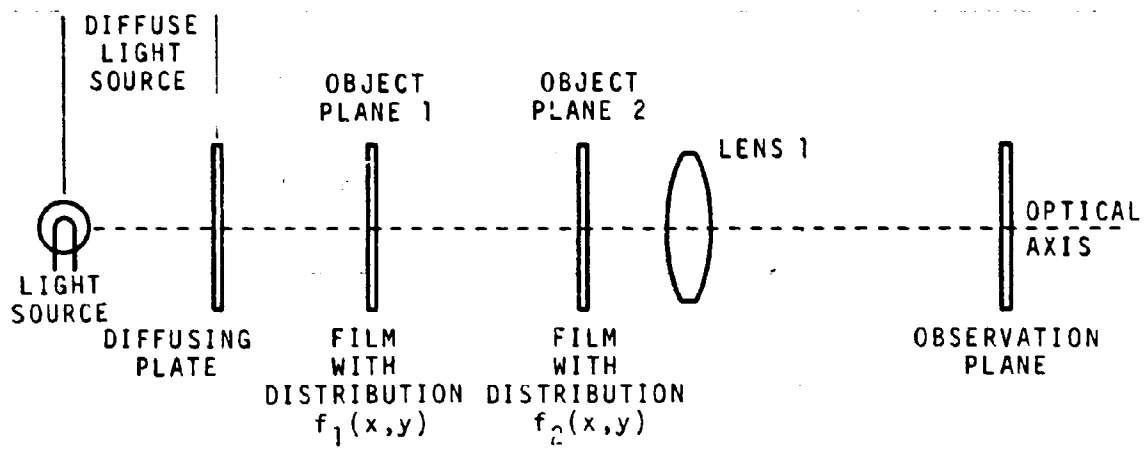


Figure 21. Basic Space Incoherent Information Processor [11]

It should be noted that in the system just described, the diffuse light source and the first signal source may be replaced by a cathode ray tube.

Because signals are processed in two dimensions in the incoherent processor (as was the case for coherent optical processors), the information packing density is quite high. Many signals may be processed in parallel without the size or complexity of the system increasing.

One feature of the optical correlator which is of interest in radar range measurements is space delay. If the second signal  $f_2(x,y)$  is shifted in the  $x$  or the  $y$  plane, a proportional shift will be observed in the correlation function at the observation plane. The delayed signal from the radar is recorded as a proportional space delay in  $f_2(x,y)$ . The position of the correlation function peak determines the time delay.

### 1.3 Mathematical System Modeling for Computer Simulation

#### 1.3.1 Intermediate Frequency Amplifier Simulation

##### 1.3.1.1 Introduction

This task is a continuing effort to obtain a digital computer simulation of a radar system. This section discusses the simulation of a linear IF amplifier in cascade with several nonlinearities.

##### 1.3.1.2 Mathematical Development

The IF amplifier is shown schematically in Figure 22. The unity gain amplifiers are shown to indicate impedance isolation. The transfer function of the tank circuit is written down from inspection:

$$\frac{v_o}{v_i} = \frac{sL}{RLC s^2 + sL + R} \quad (19)$$

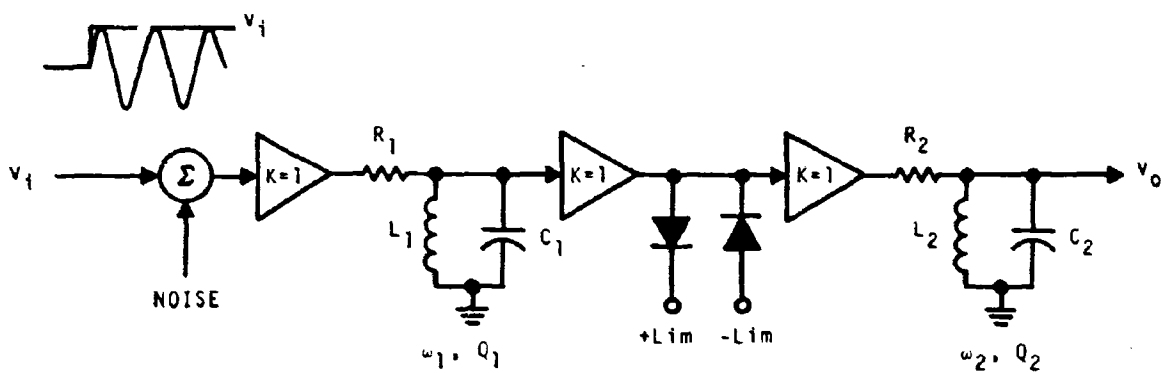


Figure 22. IF Amplifier To Be Simulated

The parameters R, L, C are computed using equations

$$\omega^2 = 1/LC \quad (20a)$$

$$Q = R/\omega L \quad (20b)$$

$$R = 1000 \text{ ohms} \quad (20c)$$

Q and  $\omega$  are designer input quantities and the value of R = 1000 was arbitrarily chosen as a practical value for transistor circuits. Equation (20a) is an approximation and may be in error by about 1% for low-Q circuits. This was compensated for in the program.

For the steady state frequency sweep, vector algebra is used to calculate the magnitude and phase of the first stage output for a unit amplitude sinusoidal input. This output is used as the input for the next stage. No nonlinearities are included and the input frequency is swept from  $.5f_{IF}$  to  $1.5f_{IF}$ , where  $f_{IF}$  = the intermediate frequency. The results are plotted by computer and are shown in Figure 23. No attempt was made to optimize the parameters for any specific application.

The input to the amplifier for the transient analysis was a sinusoid plus noise, such that,

$$\text{input} = 0, t < 0$$

$$\text{input} = \sin \omega_{in} t + \text{noise}, t \geq 0 \quad (21)$$

The input frequency is a read-in quantity and the noise is band unlimited with a flat distribution. The problem is allowed to run for 10 cycles of the input frequency. The differential equations for the filters are:

$$RLC \dot{v}_o = L\dot{v}_i - L\dot{v}_o - Rv_o$$

$$\dot{v}_o = \int \ddot{v}_o dt$$

$$v_o = \int \dot{v}_o dt \quad (22)$$

There is no unique integration procedure for solving these equations on a digital computer. Based on past experience, the input sinusoid was divided into 60 parts (.5 nanosec. in width for a 30 MHz IF) and a combined Euler and Modified Euler integration algorithm was used. Equations (21) and (22) were evaluated and the results stored on a magnetic disk. A

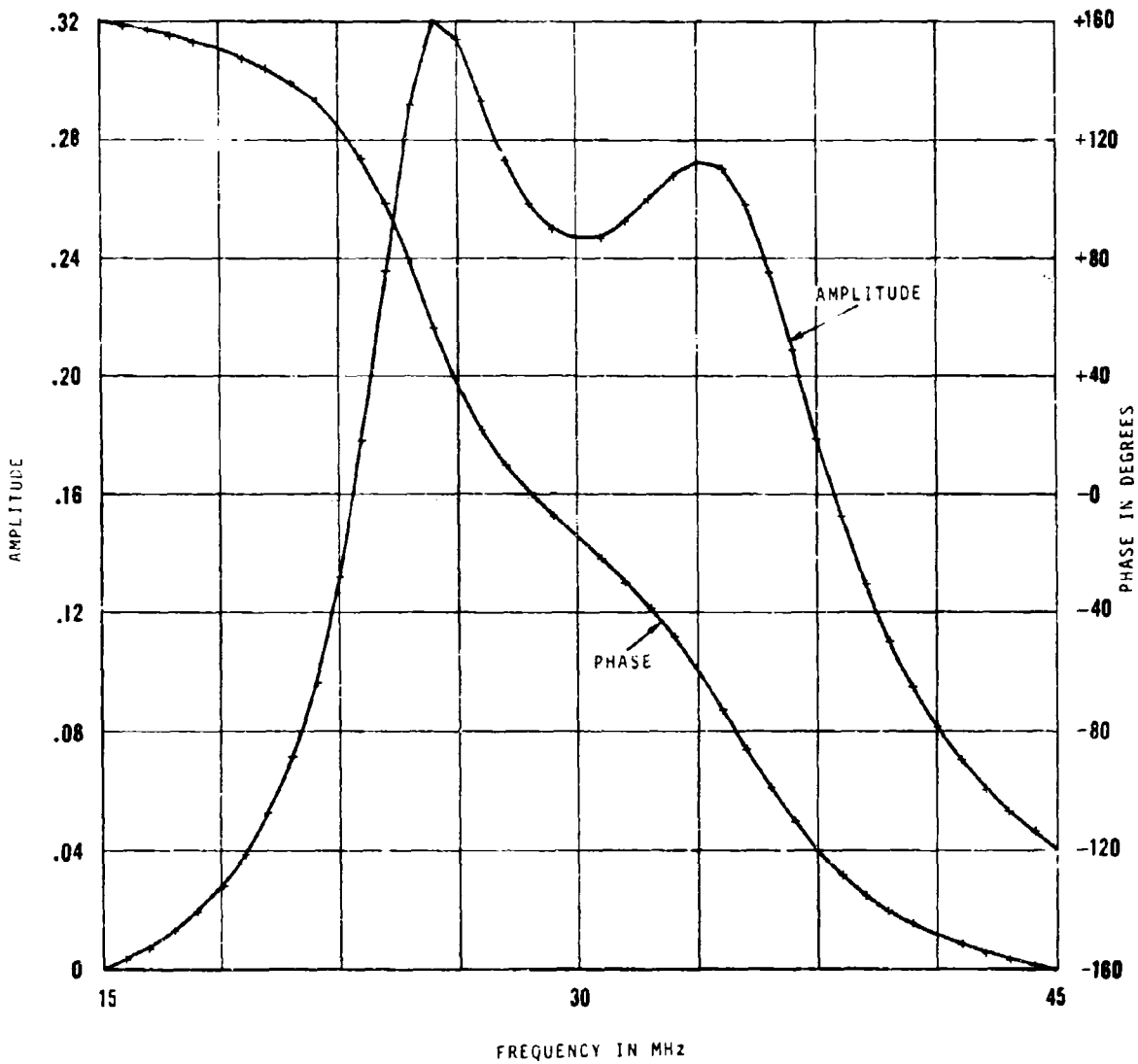


Figure 23. Steady State Frequency Response of a Two Stage IF Amplifier Without Limiting for  $f_{I.f.} = 30$  MHz;  $f_1 = 35$  MHz;  $Q_1 = 5$ ;  $f_2 = 25$  MHz;  $Q_2 = 6$

logic subroutine limited the input to the second filter. Figure 24 is a plot of the noisy input, Figure 25 is the output of the first filter, Figure 26 is the output of the second filter. All the graphs are plotted to the same scale and can be superimposed. After the computation is complete, the stored values are retrieved from the disk. The program stores the maximum and minimum values of the outputs and automatically scales the plot.

### 1.3.2 Rectangular Aperture Simulation

#### 1.3.2.1 Introduction

This section describes the digital simulation of the radiation pattern emanating from a rectangular aperture. The aperture can be a waveguide feedhorn or a linear planar array. The results of this simulation can be used as a design tool and also serve as the first step in the analysis of a multi-element (lenses and reflectors) antenna.

#### 1.3.2.2 Mathematical Development

The field strength at a point "P" as a result of a radiating source is given by [12],

$$U_p = \frac{1}{4\pi} \int_A F(\xi, \eta) \frac{e^{-j2\pi \frac{r}{\lambda}}}{r} \left[ \left( \frac{2\pi j}{\lambda} + \frac{1}{r} \right) \vec{i}_z \cdot \vec{r}_1 + \frac{2\pi j}{\lambda} \vec{i}_z \cdot \vec{s} \right] d\xi d\eta \quad (23)$$

See Figure 27 for the definition of coordinate systems and variables. If the far field pattern is of primary interest, equation (23) can be simplified to:

$$U_p = \frac{j}{\lambda R} e^{-j\frac{2\pi R}{\lambda}} \int_A F(\xi, \eta) e^{j\frac{2\pi}{\lambda} \sin\theta (\xi \cos\phi + \eta \sin\phi)} d\xi d\eta \quad (24)$$

Physically, equation (24) assumes that:

- a.  $\vec{R}_1 = \vec{r}_1$
- b. All regions of the aperture are excited in time phase
- c. Most of the energy is concentrated near the z axis where  $\cos\theta=1$

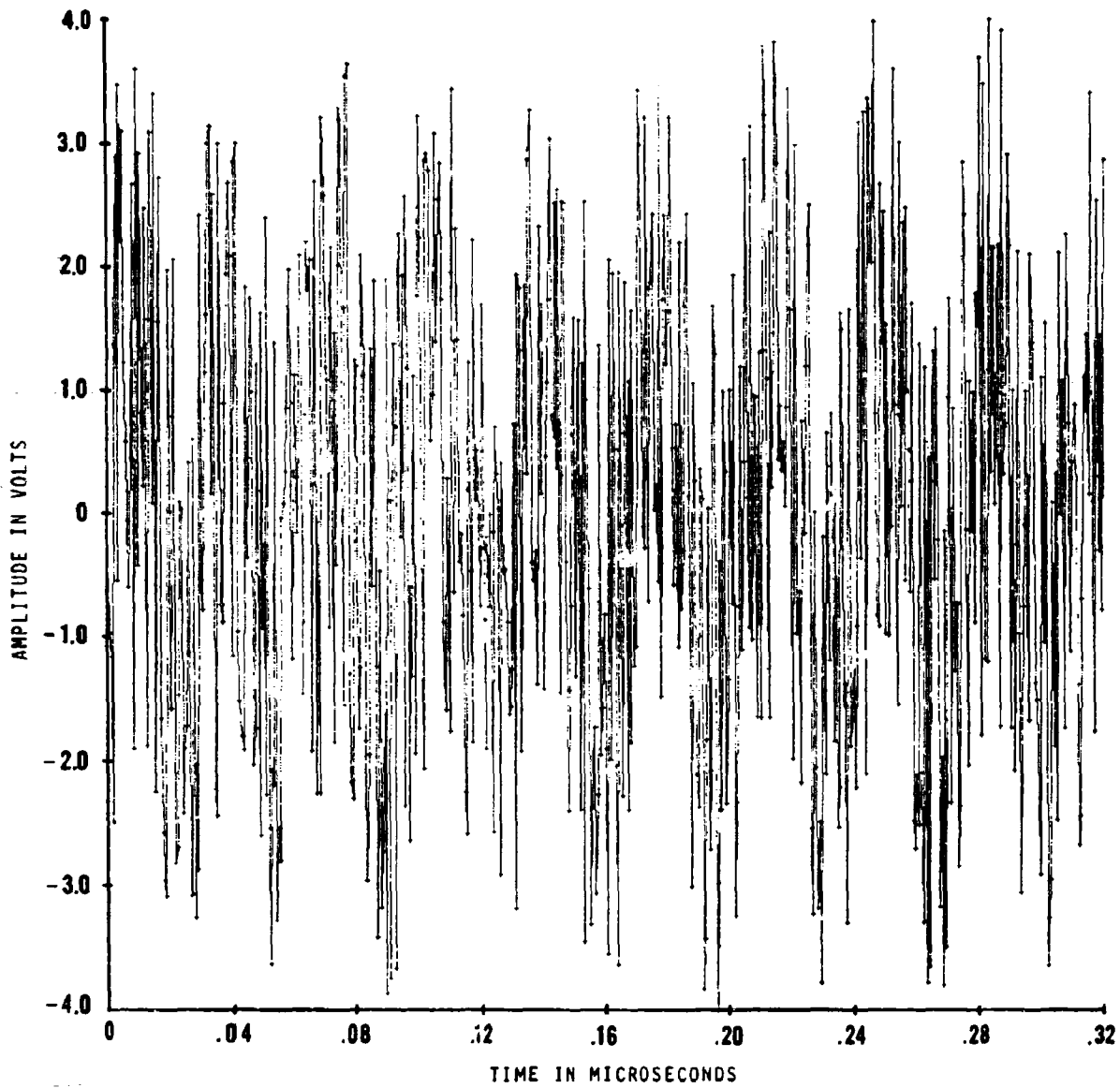


Figure 24. Noisy Sinusoidal Input  $V = \sin \omega t + \text{noise}$ ,  
for White Noise of Zero Mean and Unity  
Variance

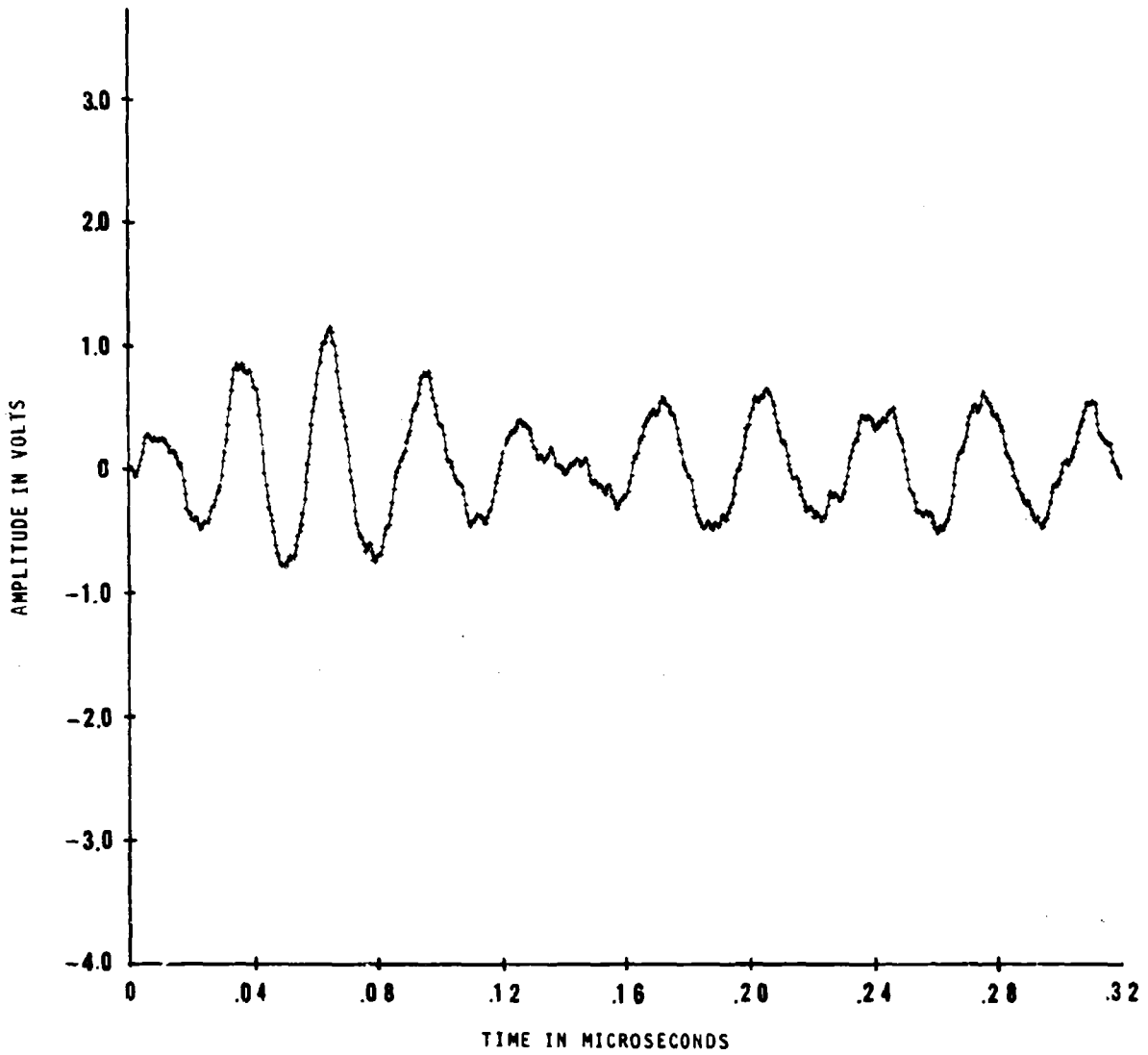


Figure 25. Output of First Stage of IF Amplifier

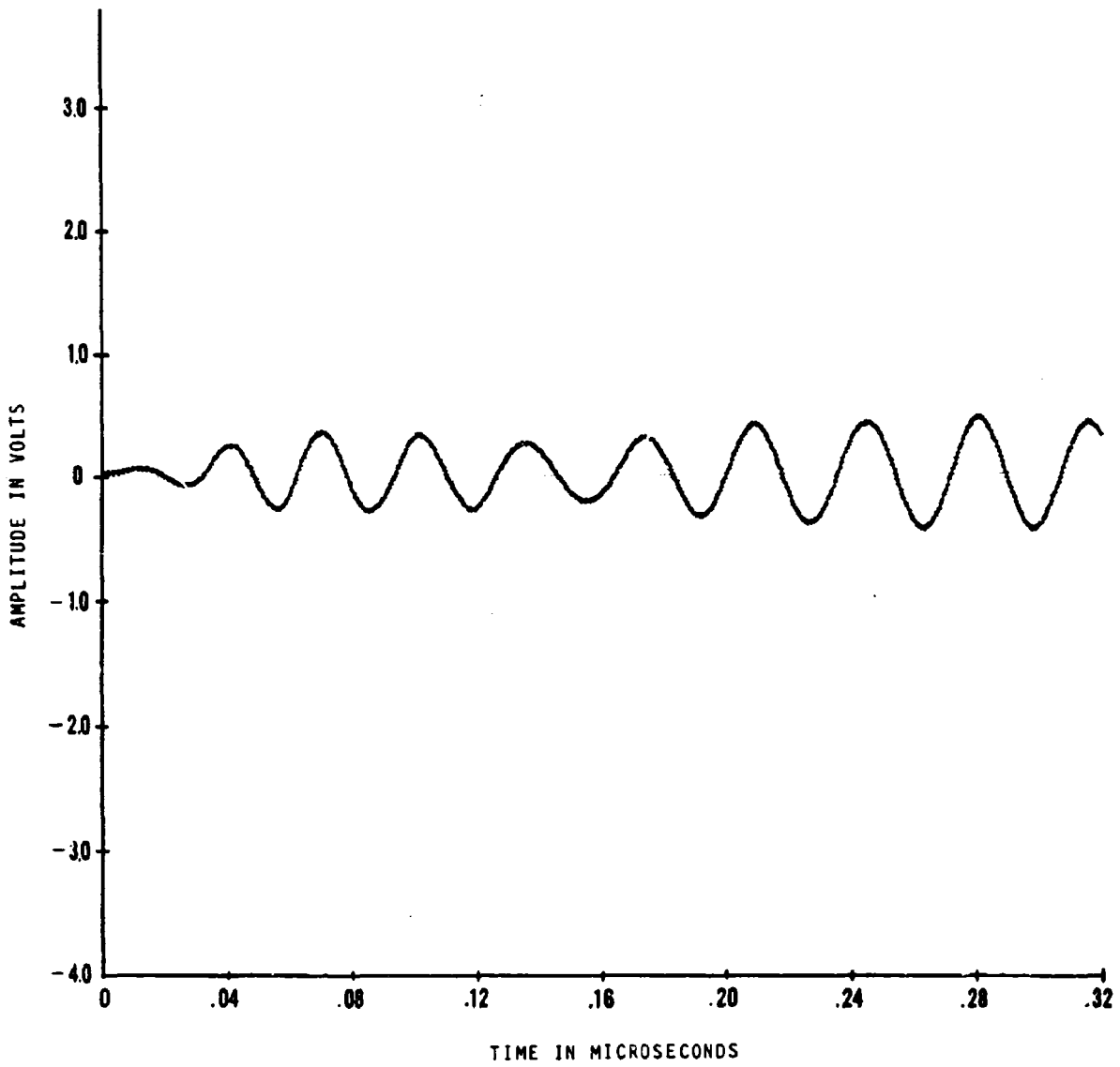


Figure 26. Output of Second Stage of IF Amplifier

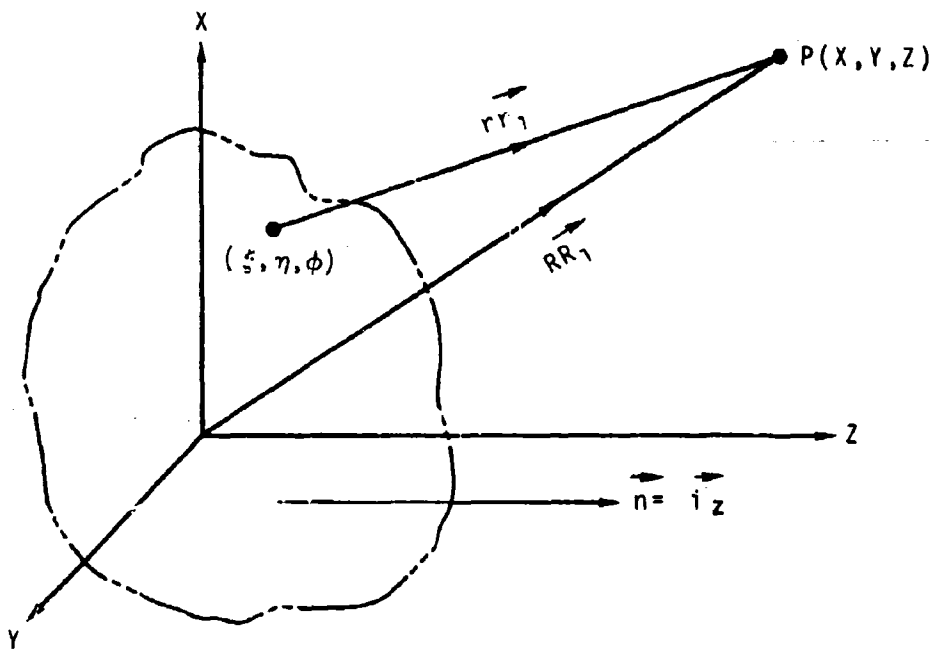


Figure 27. Radiation Coordinate System

Finally, if only the relative pattern amplitude is of interest, the equation reduces to:

$$U_p(\theta, \phi) = \int_{-b/2}^{b/2} \int_{-a/2}^{a/2} F(\xi, \eta) e^{\frac{j2\pi}{\lambda} \sin\theta (\xi \cos\phi + \eta \sin\phi)} d\xi d\eta \quad (25)$$

Figure 28 shows the spherical coordinate system used.  $\theta$ , and  $\phi$  are normal spherical coordinate angles with  $\phi$  representing a rotation about the normal to the aperture plane and  $\theta$  a rotation with respect to Z about the Y' axis. When  $\phi = 0^\circ$ ,  $\theta$  is in the principal plane, XZ (H plane), and when  $\phi = 90^\circ$ ,  $\theta$  is in the YZ plane, (E plane).

#### 1.3.2.3 Computational Procedure

Using some relatively simple expressions for  $F(\xi, \eta)$ , equation (25) can be integrated and solved in closed form. It is these solutions which served as a check on the computer evaluation. Of course, a computer performs quantized numerical integration but is able to evaluate almost any complex integrand and sum the integrand with vanishingly small error. When the computer procedure checks a closed form integral evaluation, it can reasonably be inferred that the computer program is valid for integrands which cannot be solved in closed form.

The procedure used in this problem was to conceptually visualize the aperture partitioned into small squares (see Figure 29). At the center of each square, a one-way isotropic radiator was placed and scaled so that the total energy and energy distribution in the aperture was unchanged. After an angle  $\phi$  was selected, the integral was evaluated at 50 values of  $\theta$  (from  $0 \leq \theta \leq 5a/\lambda$ ).

#### 1.3.2.4 Evaluation of Results

Figures 30 and 31 are computer plotted field patterns of a rectangular aperture with  $\lambda/a = .1$ . The curves are identical except that Figure 30 has a linear voltage ordinate and Figure 31 is plotted in db. The aperture excitation is

$$F(\xi, \eta) = \cos\left(\frac{\pi}{a} \xi\right) \quad (26)$$

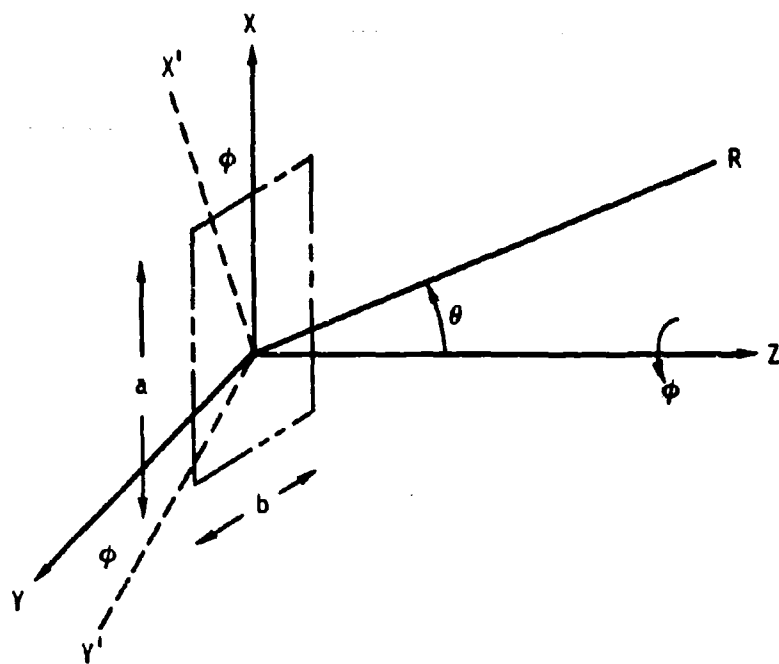


Figure 28. Spherical Coordinates

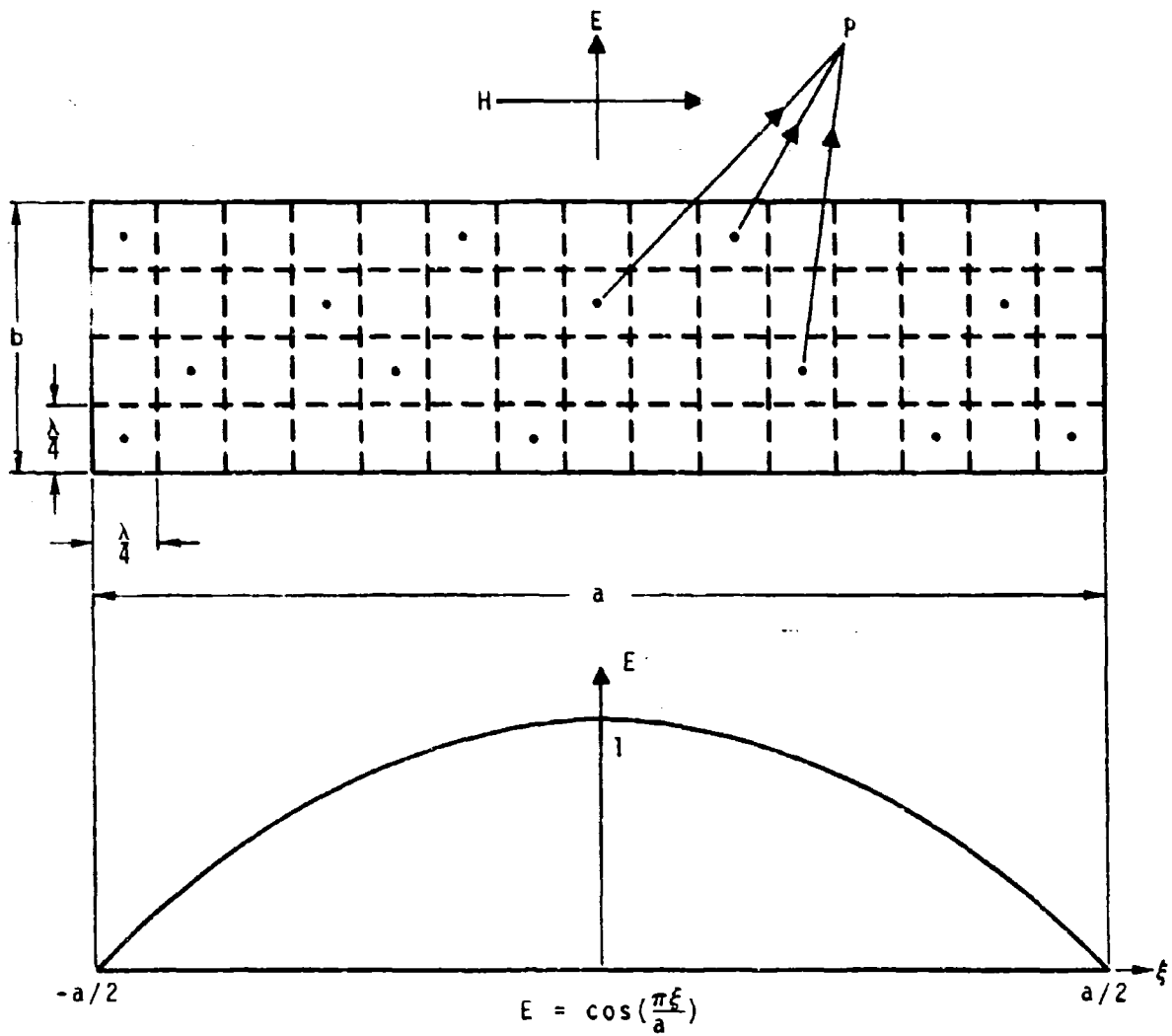


Figure 29. Aperture Partitioning and Excitation

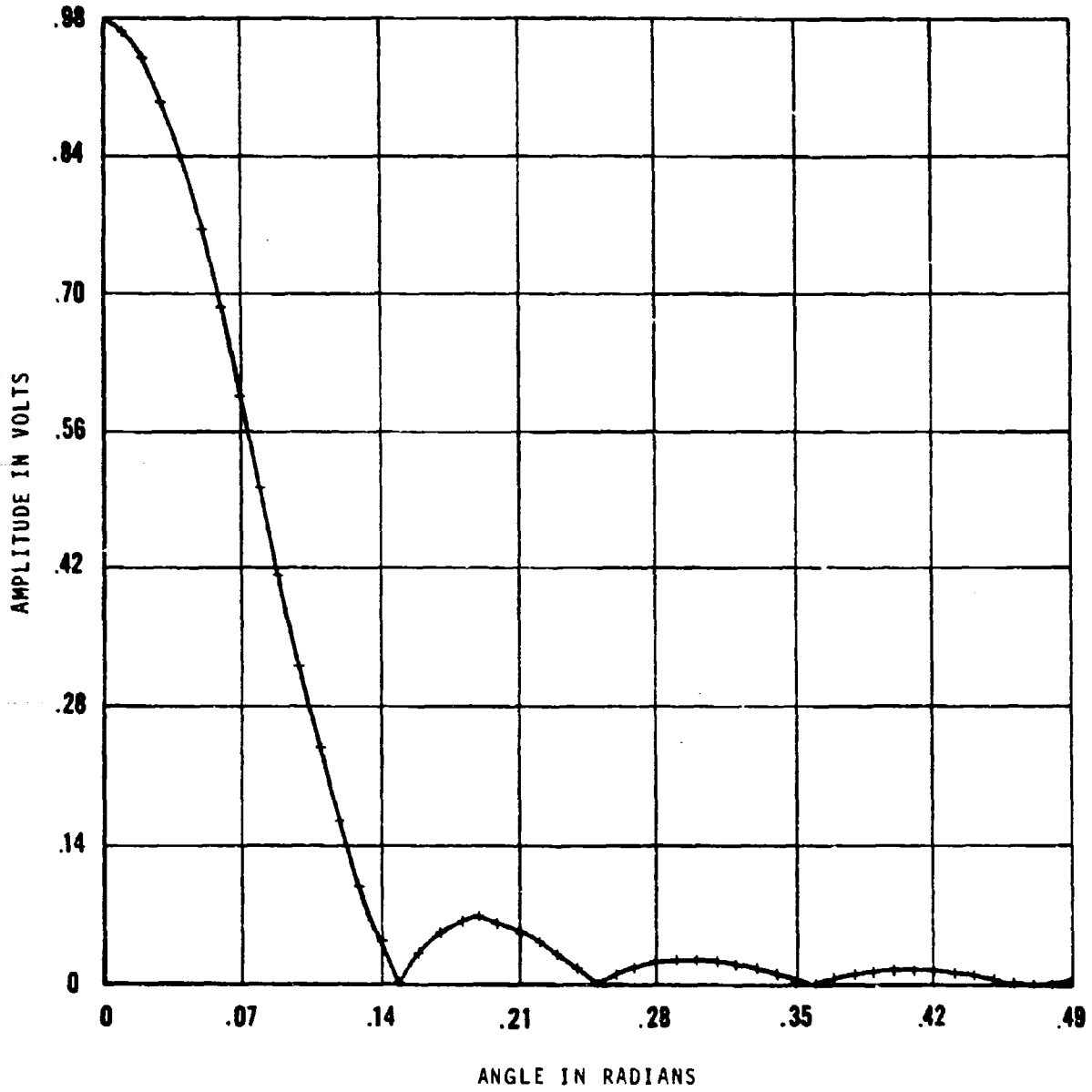


Figure 30. H-Plane Field Intensity Pattern.  
 Cosine Excitation with  $\frac{\lambda}{a} = 0.1$ , and  
 Linear Scaling.

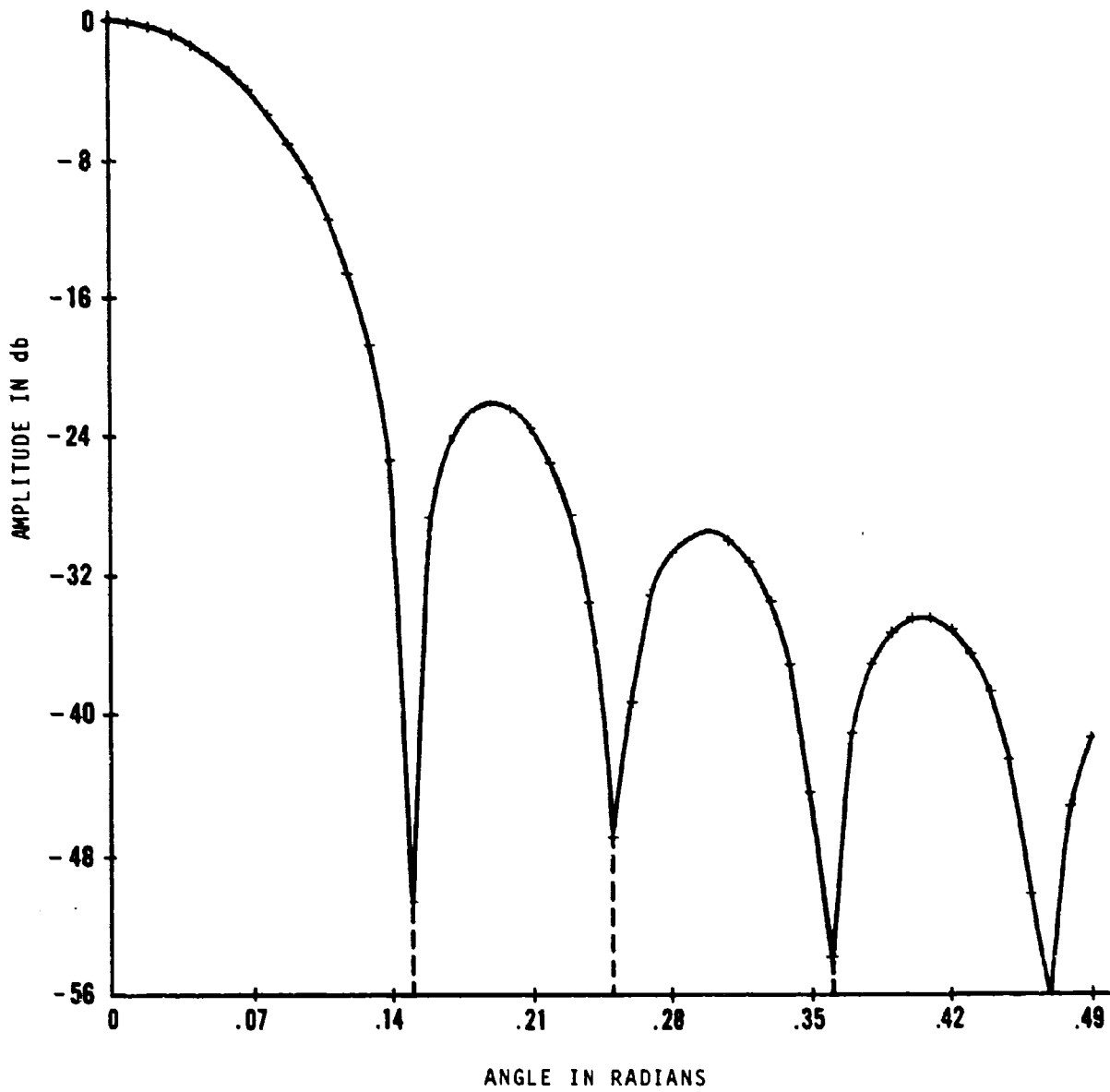


Figure 31. H-Plane Field Intensity Pattern.  
 Cosine Excitation with  $\frac{\lambda}{a} = 0.1$ , and  
 db Scaling.

which is the easiest way to excite an aperture. The excitations are uniform (independent) with  $n$ . All output values are normalized to unity or zero db. The following table shows the excellent agreement between the results achieved and the textbook values.

Table I

	<u>Computer Results</u>	<u>Textbook Values</u>
Half Power Beam width	.06 rad (.6 $\lambda/a$ )	.6 $\lambda/a$
# of first zero	.15 rad = 1.5 $\lambda/a$	1.5 $\lambda/a$
First side-lobe intensity	-23 db	-23 db
Phase distortion	(zero, odd lobes $\pi$ , even lobes (from printed listing))	(zero, odd lobes $\pi$ , even lobes)
Separation of zeros	.105 rad =1.05 $\lambda/a$	$\lambda/a$

Figures 32 through 35 are representative of a small rectangular waveguide feeding a large dish. The following information can be extracted from these curves.

- a. In the "H" plane, the beam width is 1.2  $\lambda/a$  which agrees with standard textbooks.
- b. In the "E" plane, the beam width is .94  $\lambda/a$  (correct value = .88  $\lambda/a$ ).
- c. The first zero in both planes occurs at 90°.
- d. However, the energy distribution at large values of  $\theta$  appears to be incorrect. The reason for this error is that the original equation assumed that the majority of the energy was concentrated normal to the aperture. This assumption is not valid for small apertures.

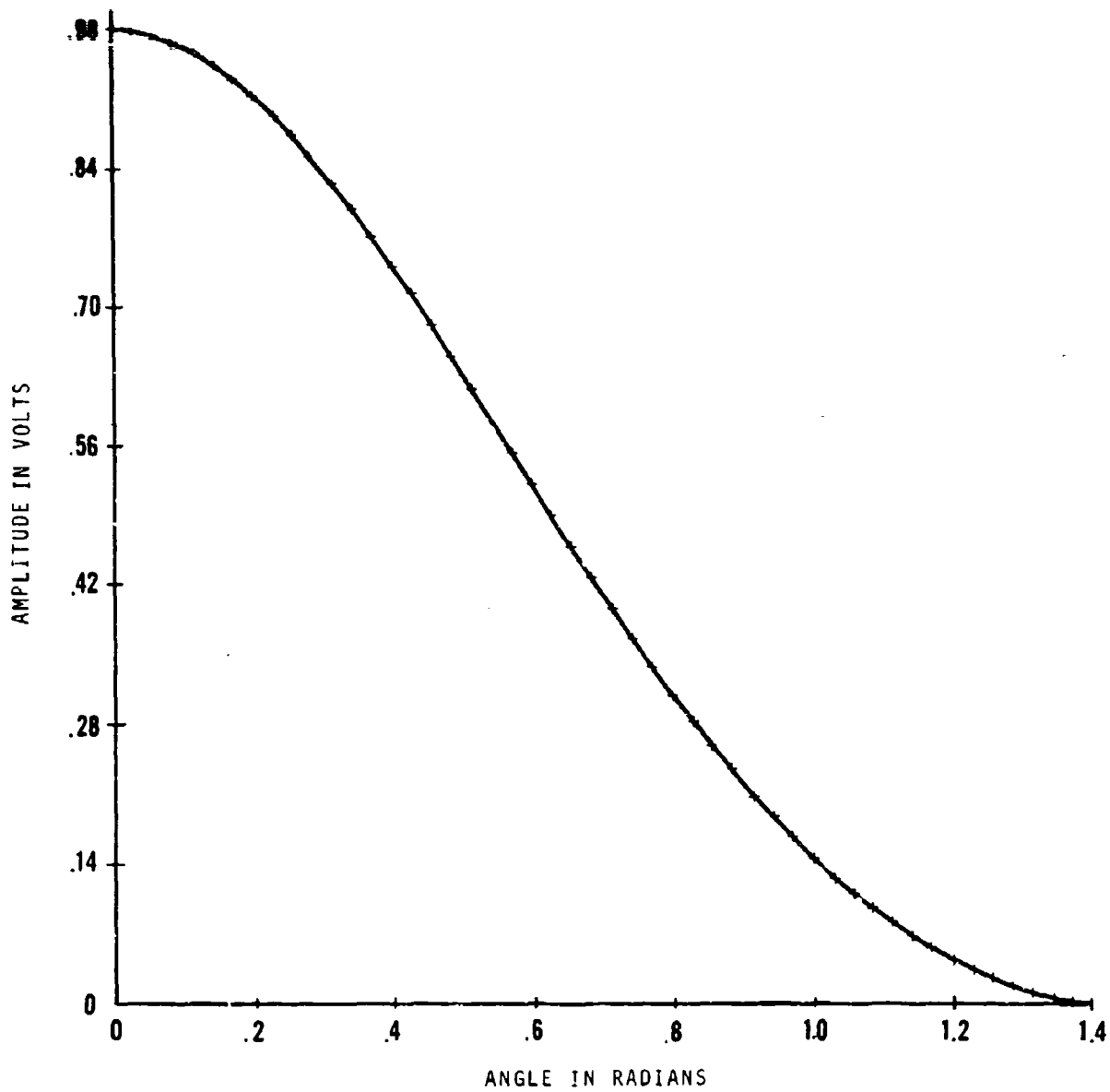


Figure 32. Voltage H-Plane Pattern for a Cosine Excitation with  $\frac{\lambda}{a} = 1$ , and Linear Scaling.

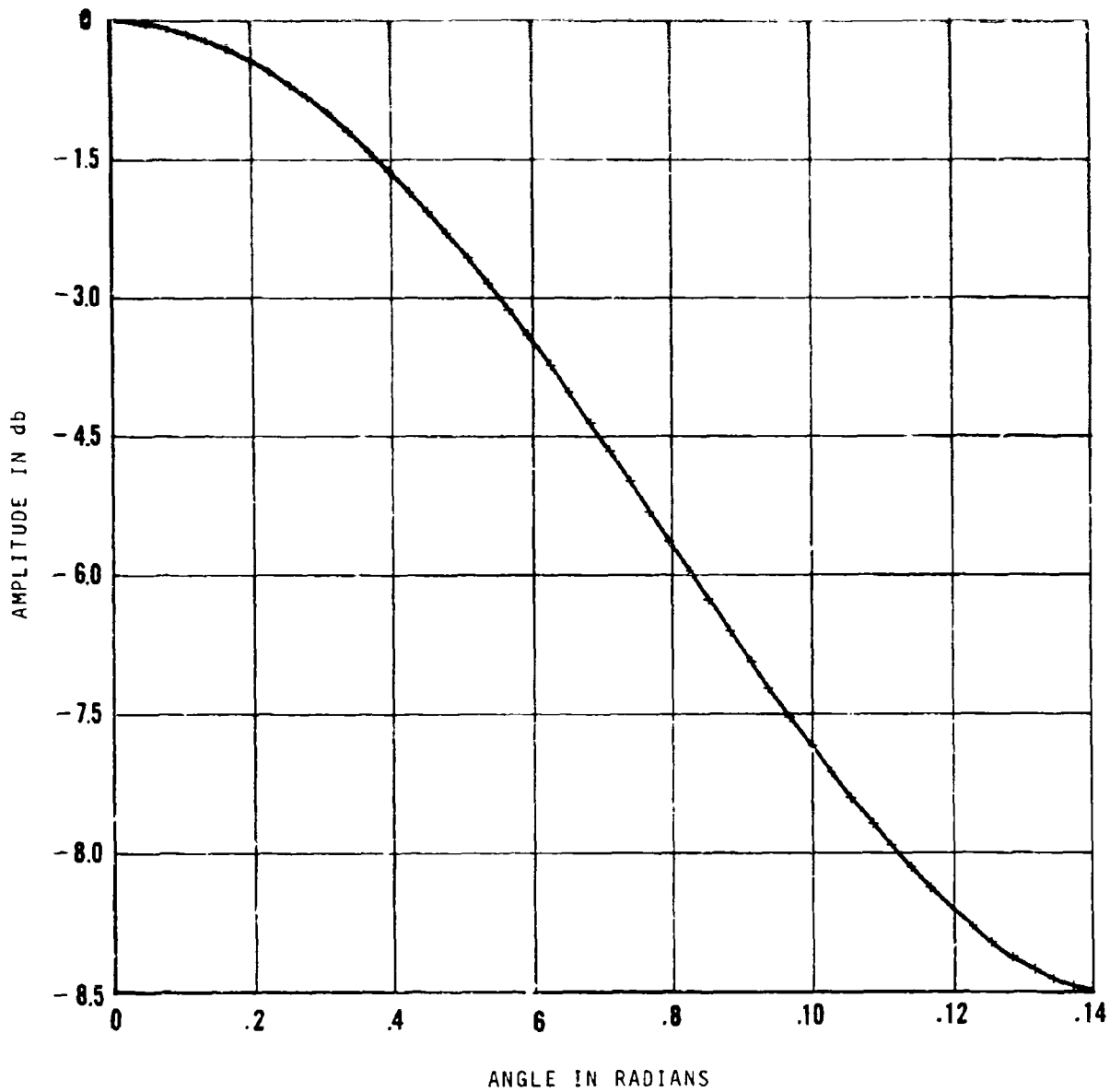


Figure 33. H-Plane Antenna Pattern for  $\phi = 0$ .  
 Cosine Excitation with  $\frac{\lambda}{a} = 1$ , and  
 db Scaling.

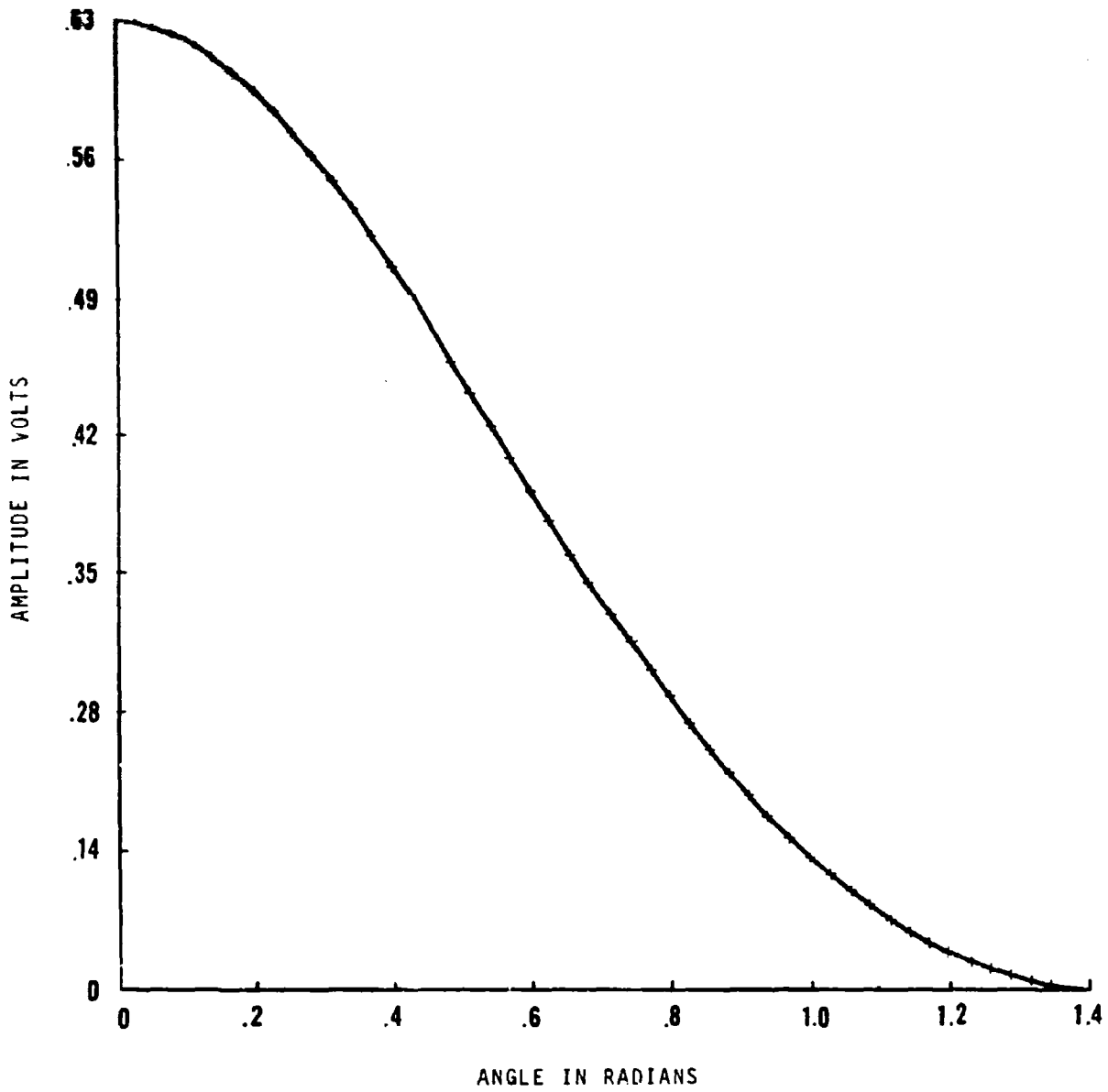


Figure 34. E-Plane Antenna Pattern for  $\phi = \pi/2$ .  
 Uniform Excitation with  $\frac{\lambda}{b} = 1$ , and  
 Linear Scaling.

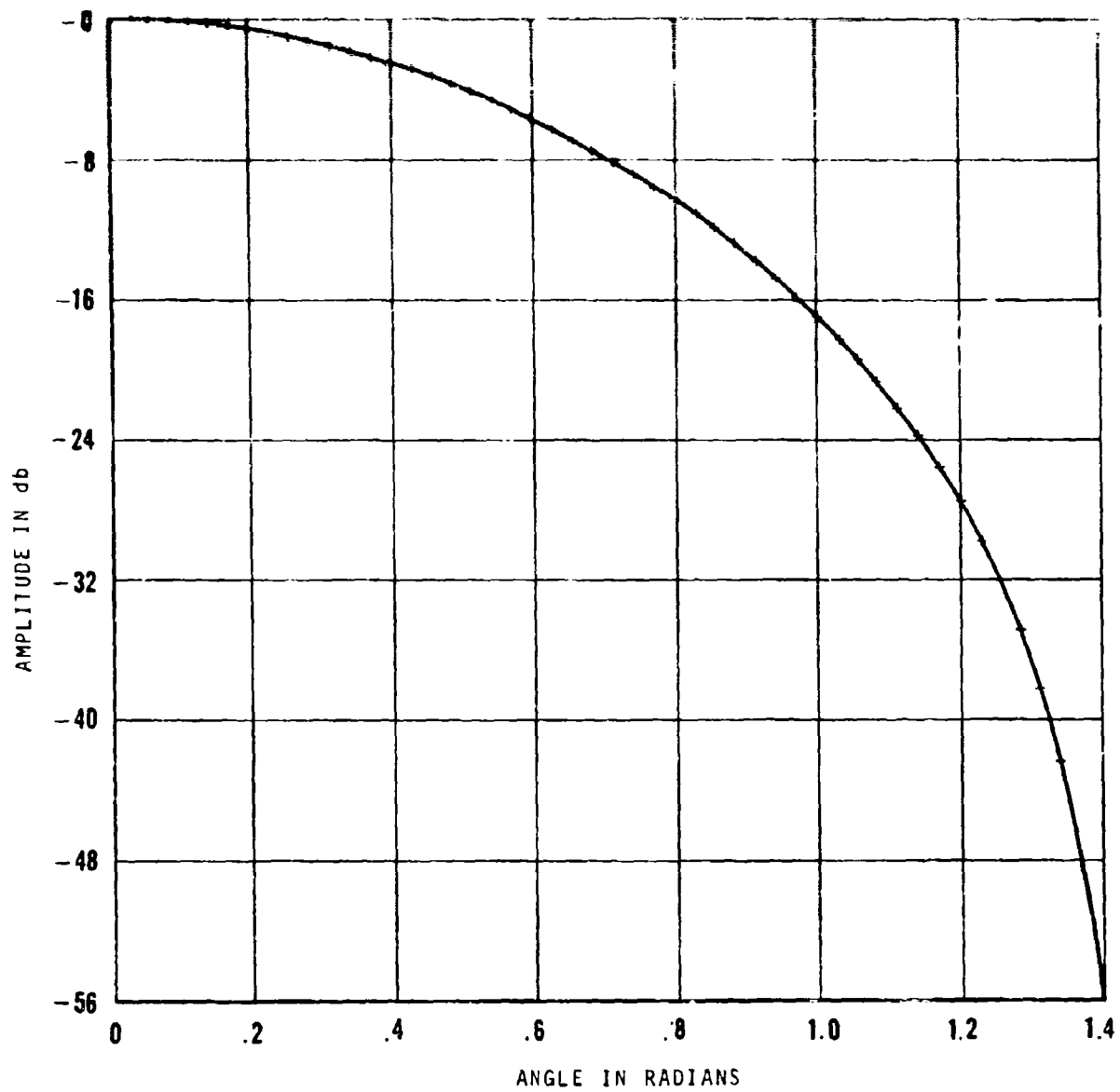


Figure 35. E-Plane Antenna Pattern for  $\phi = \pi/2$ .  
 Uniform Excitation with  $\frac{\lambda}{b} = 1$ , and  
 db Scaling.

#### 1.3.2.5 Summary

The concept of computing the radiation pattern of a radiating area by subdividing it into a large number of equivalent isotropic radiators appears to be valid. This simulation should be considered as only the first step and can be extended to include small apertures, circular apertures, phased arrays, reflectors, lenses, and multiple elements.

#### 1.4 Experimental Millimeter Radar

The statistical analysis of radar data obtained at Ballistics Research Laboratory, Aberdeen, Maryland, has been completed and the probability density functions are presented. The data has been correlated with the power spectral densities published in ECOM-01253-2 to furnish a complete statistical picture of several objects at 70 GHz. The millimeter radar has been completed and is described in detail. Initial experiments have indicated that the system is very stable and can be used for reliable clutter and obstacle measurements. Data taken with the radar at 70 GHz is published and pertinent characteristics are discussed.

##### 1.4.1 Radar Design

Construction of an active radar system, operating at 70 GHz was completed during the past quarter. The system has undergone tests and is currently being used for measurements being performed in support of the study program. Portions of the system and the progress in its construction were described in Technical Reports ECOM-01253-1 and ECOM-01253-2. Some system design details not described before, as well as actual system test data, are reported here. A photograph of the system is given in Figure 36.

Significant improvements in the fabrication techniques for the BL-234C magnetron were evolved by the design engineers at the Bomac Division of Varian Associates during the past quarter. Failure analyses performed by Bomac on earlier tubes delivered to Harry Diamond Laboratories and to Norden, have led to revised cathode and magnet activation techniques. The magnetron finally delivered for use in the Norden system has exhibited excellent characteristics in terms of mode width and stability. The peak power output of the magnetron was measured in excess of 900 watts. The frequency of operation was measured to be 70.42 GHz.

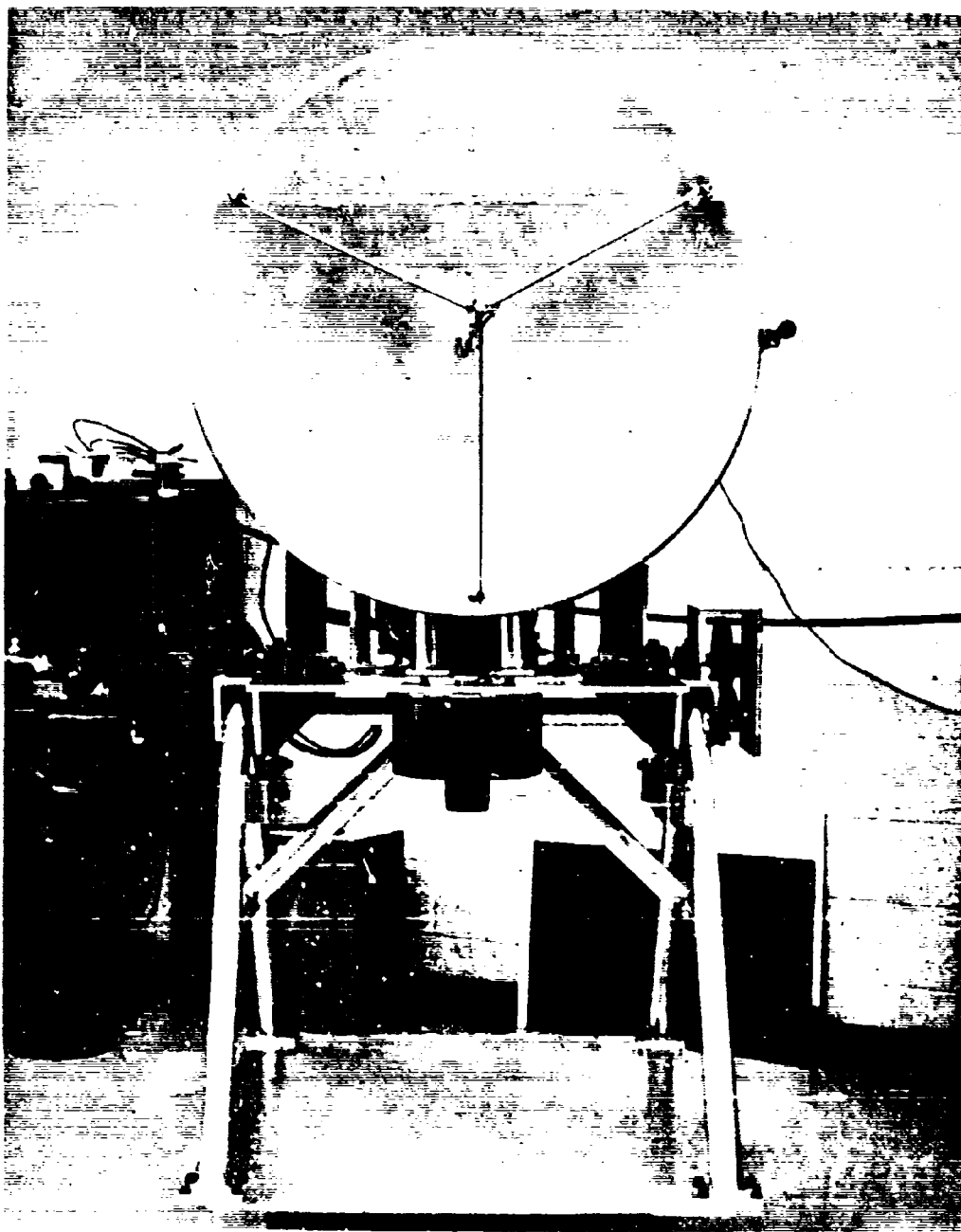


Figure 36. Experimental Millimeter Radar

The BL-S-517 crystal-protecting TR tube, also manufactured by Bomac, was tested prior to installation in the system and the following significant data was obtained:

Recovery time: approx. 0.2 microsecond  
Spike energy leakage: 0.04 erg  
Insertion loss on receive: 1 db

With no apparent crystal degradation over the first few hours of system operation, it appears that the protection offered by the BL-S-517, is adequate for the particular 1N2792 crystals currently in use.

Waveguide losses in the transmit direction from the magnetron flange to the input of the antenna feedhorn run were found to be 3.1 db. The losses in the receive direction from the feedhorn flange to the mixer input were measured at 4.2 db. The feedhorn run adds approximately 0.6 db to the system losses in each direction.

Some experimentation with a simple choke design will be carried out in an effort to reduce the system losses at each flange junction. Nine such junctions are included in each signal direction.

The system contains a variable PRF generator with outputs at 2, 3, and 5 kHz. An externally controlled PRF option is also available. Solid state devices are used throughout the PRF generator as well as in the system internal power supplies. Relay provisions for warm-up time delay, modulator protection, and magnetron filament power reduction in the transmit mode have been made.

A relatively novel approach was taken in the design of the system modulator. Some experiments were performed with a free-running blocking oscillator which pulsed the magnetron directly. Tests revealed this scheme to be lacking in flexibility and reliability, particularly when employed with a magnetron characterized by a narrow mode width and critical dependence on the voltage rate of rise of the modulating pulse. A hard tube modulator with rapid rise capability and stable output was therefore selected to drive the magnetron. The input for this modulator stage is obtained from a series of avalanche transistors which are driven into their avalanche mode of operation by the trigger input from the PRF generator. The rate of rise of the pulse output of the avalanche circuitry is controllable to some degree by adjustment of the terminating impedance. The pulse width is controlled by the length of the delay line whose charge feeds the energy into the avalanche transistors. The avalanche output of roughly 150 volts exhibits

typical rise times of 2 nanoseconds. Modulator pulse widths from 20 to 60 nanoseconds have been obtained.

The hard tube modulator approach using the avalanche transistor driver has resulted in stable and repeatable RF operating conditions, requiring little or no modulator voltage adjustments on a day-to-day basis. The additional volume and power required by the avalanche circuitry is relatively insignificant in comparison to the improvement in operating reliability.

System amplitude stability was verified by boxcarrying the video return from a solid, isolated target (tall smoke stack) located at 31 microseconds in range, see Figure 44. A low frequency analysis performed on this boxcarred signal output failed to show any low frequency scintillation content which could be attributed to instabilities in the radar. A similar low frequency spectrum analysis was carried out on the returns from bare trees, see Figure 39, at roughly 2 microseconds in range. It disclosed a low frequency scintillation content extending to only 25 Hz. This is considerably less than the 300 Hz extent of scintillation frequencies obtained in spectrum analyses performed against trees in full foliage at Ballistics Research Laboratories, Aberdeen, Maryland in the summer of 1965. (See ECOM-01253-2, Appendix C)

#### 1.4.2 Experimental Results

A series of preliminary experiments have been conducted using the experimental radar described in section 1.4.1. The data was obtained at the nominal pulse width of 60 nanoseconds and at the narrower pulse width of 20 nanoseconds.

Figure 37 shows the 60 nanosecond transmitter pulse at a power level of 900 watts (peak). The shape of pulse is quite square. The ringing is due primarily to the measurement circuitry.

Figure 38 shows the return from a large tree with no foliage. The return is quite strong and relatively steady. Figure 39 shows the power spectral density of this return. Note also the steady peaked return of Figure 38 which subtends approximately 200 ns., i.e., 100 feet, in range. This is much larger than the tree dimension.

Figure 40 shows the discrete return from an aluminum cable.

Figure 41 shows the return from a large tree, and again, has the distinguishing twin peaks as in Figure 38.

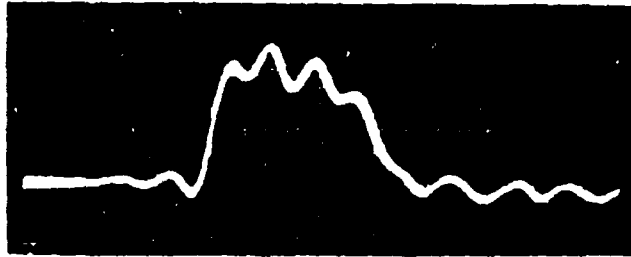


Figure 37. 60 ns Pulse, Transmitted at a Peak  
Power of 900 watts (Time scale = 20 ns/cm)

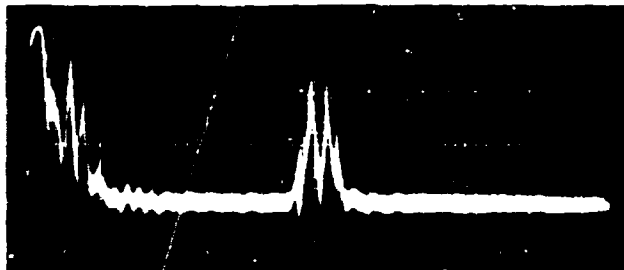


Figure 38. Return from a Tree with No Foliage  
(Time scale = 200 ns/cm)

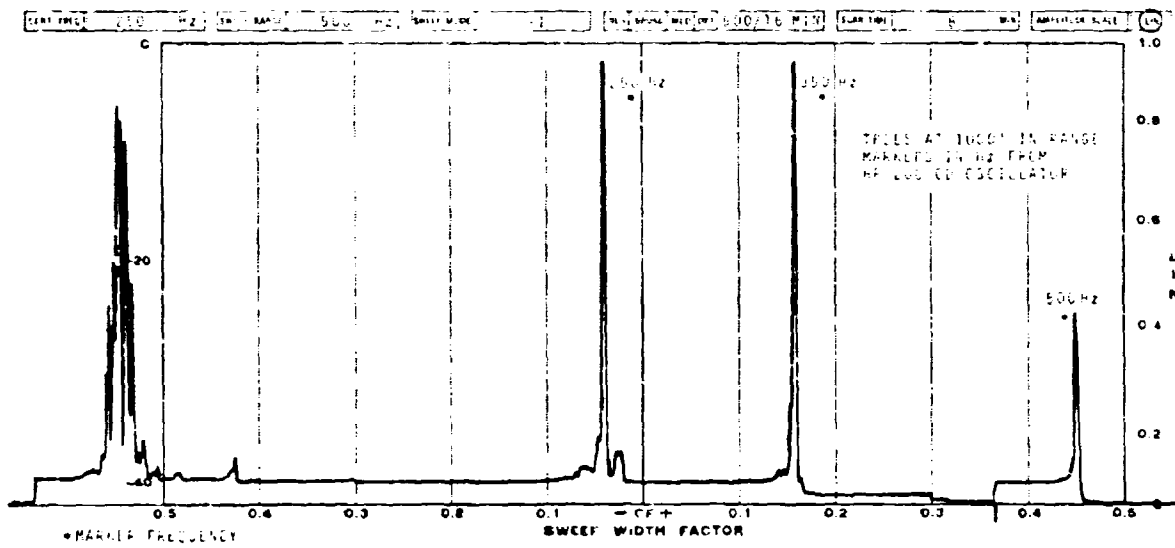


Figure 39. Clutter Spectrum from Trees at 1000 Feet in Range

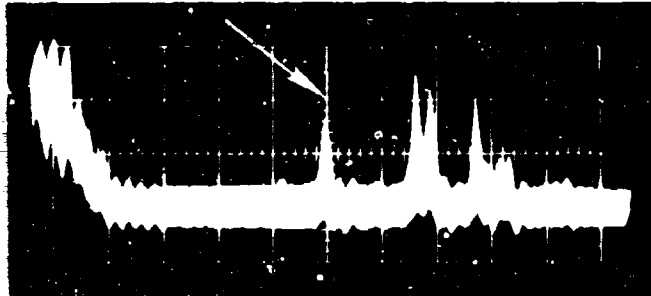


Figure 40. Return from an Aluminum Cable  
(Time scale = 200 ns/cm)

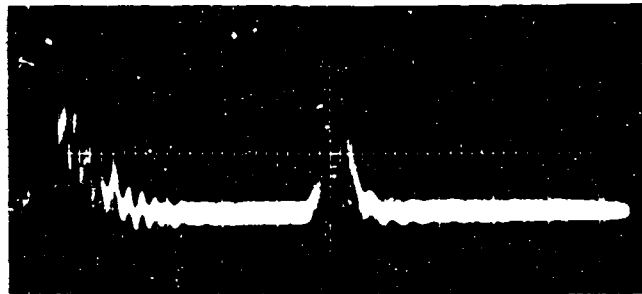


Figure 41. Return from a Tree with No Foliage  
(Time scale = 200 ns/cm)

Figure 42 shows the return from a wooden house, or more explicitly, from the metal gutters on the house.

Figure 43 shows the return from a 30-foot telephone pole. The return is extremely steady. A similar return has been observed from a brick chimney at a range of 2.9 miles. The width of the return in each case is essentially the pulse width, 60 ns. The power spectrum of the chimney is shown in Figure 44. The spectrum is almost white with very little low frequency scintillation.

Figure 45 shows the narrow pulse shape, 20 nanoseconds.

Figure 46 shows the return from a house using the narrow pulse. Note the marked decrease in clutter level compared to Figure 42.

A series of experiments, to obtain data from a variety of cables and towers, is planned for the next quarter.

### 1.4.3 Probability Densities of Experimental Data

#### 1.4.3.1 Introduction

A program of millimeter-wave radar experiments, initiating our investigation of the radar returns from clutter targets, was carried out at the Ballistics Research Laboratories, and is fully described in Appendix C of Technical Report ECOM-01253-2, March, 1966.

We are presently concerned with obtaining a description of such video returns in terms of their power spectral density and probability density function. The boxcarred, radar-video signal under investigation was either recorded with a Precision Instruments tape recorder for later analysis with respect to the signal's probability density function or analyzed immediately with respect to its power spectral density by means of a Panoramic Subsonic Analyzer. The results of the power spectral analysis were reported in the previously referenced technical report. Our purpose here, is to study the probability density function of the magnitude of the clutter and composite radar returns.

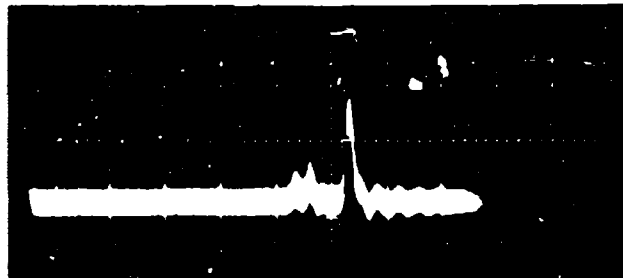


Figure 42. Return from the Metal Gutters  
on a Wooden House (Time scale = 200 ns/cm)



Figure 43. Return from a Telephone Pole  
(Time scale = 200 ns/cm)

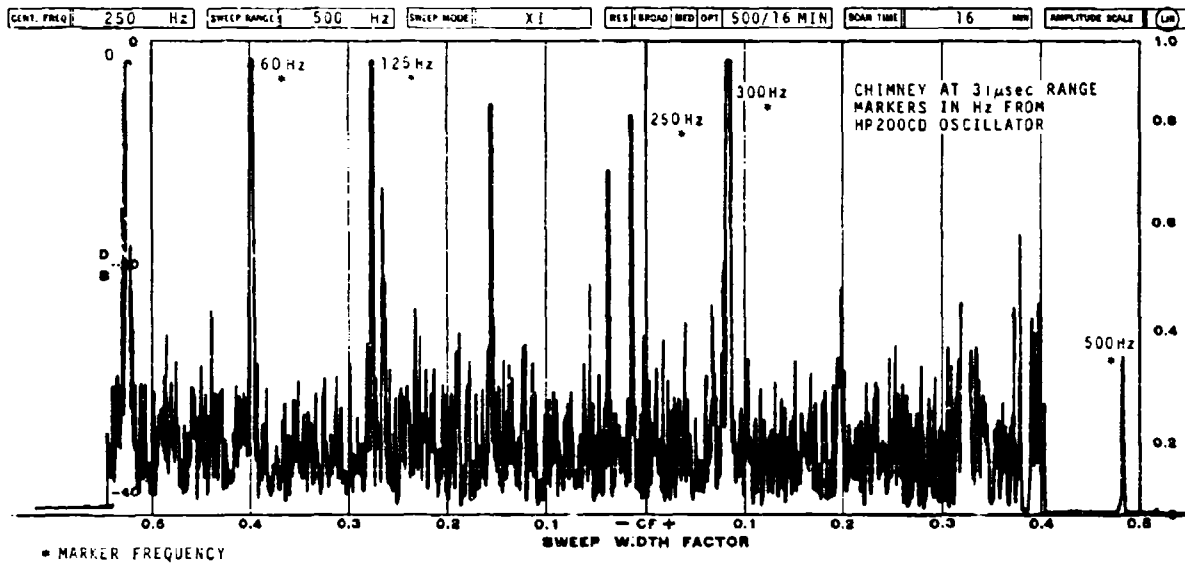


Figure 44. Radar Spectrum of Return from Chimney at 2.9 Miles in Range

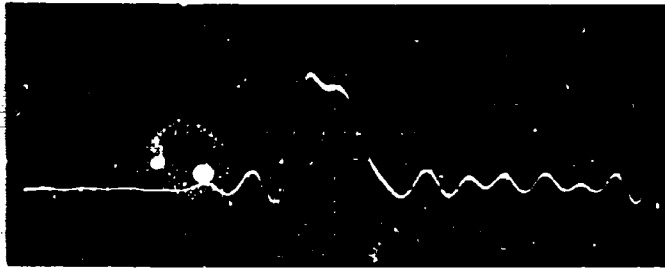


Figure 45. 20 ns Pulse (Time scale = 20 ns/cm)

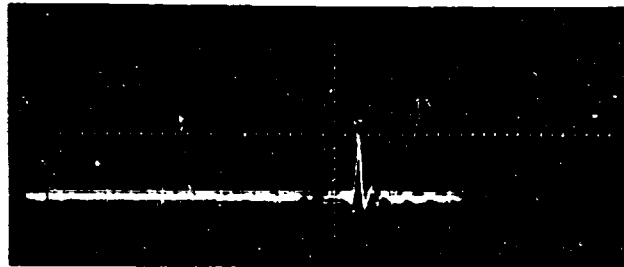


Figure 46. Return from the Metal Gutters on a  
Wooden House (Time scale = 100 ns/cm)

#### 1.4.3.2 Data Processing Techniques

The data processing work required to characterize the video signal in terms of the probability density function of its magnitude was performed at the United Aircraft Corporation computer facility in East Hartford, Connecticut. A block diagram of the system used to obtain an estimate of the probability density function is shown in Figure 47. The previously recorded, boxcarred video signal was sampled by the computer at a 1 kHz rate and sorted according to magnitude, into 200 bins, each 20 millivolts in width. The number of samples in each bin was then plotted out by the X-Y recorder. A typewriter printout of the data was also obtained. The entire operation proceeded under the supervision of the control unit.

A test run was performed in which more than  $10^4$  samples were taken of the signal

$$y = f(v) = \sin(\theta) \quad (27)$$

with  $\theta = \omega t$  and  $\omega = 1$ , at a 1 kHz rate. The experimentally determined density function,  $p(y)$ , is compared, in Figure 48, with the theoretically predictable density function

$$p_2(y) = \frac{1}{\pi} \frac{1}{\sqrt{1-y^2}} \quad [13] \quad (28)$$

The area under the experimentally determined density function has been normalized to unity. The two densities are seen to be in good agreement.

#### 1.4.3.3 Density Measurements of Radar Video

Figures 49 through 54 are reproductions of the outputs of the X-Y recorder for six different radar signals being studied. The numbers in parenthesis refer to figure numbers from Appendix C of Technical Report ECOM 0-1253-2 in which the corresponding power spectral density is displayed. Figures 49 and 50 are the probability density functions of clutter only, at two different wind velocities. Figures 51 through 53 are the probability density functions of isolated, stationary targets and Figure 54 is the probability density function of a composite target.

The area under each of the experimental curves in Figures 49 through 54 is the same, since the total number of samples taken in each case was  $2 \times 10^4$ . In order for the figures to

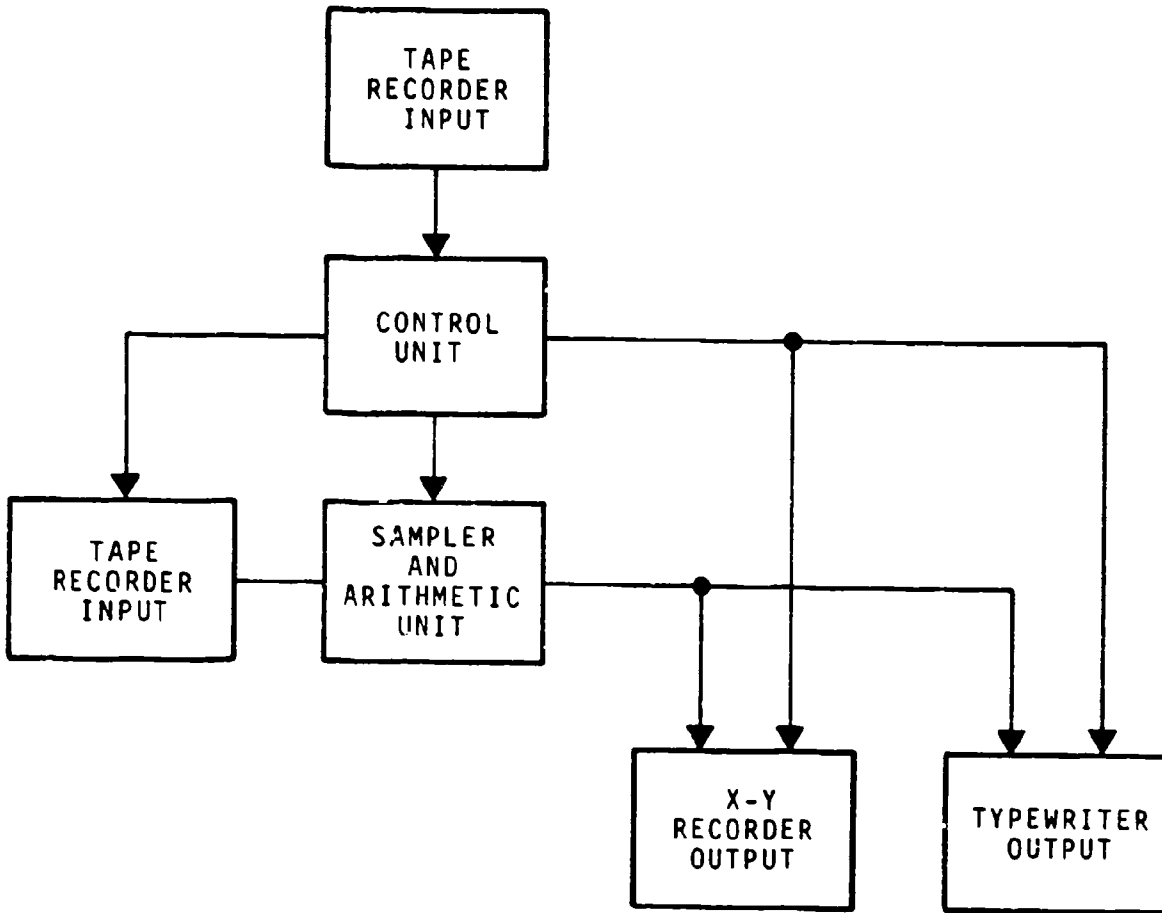


Figure 47. Block Diagram of the System Used to Obtain Estimates of the Probability Density Function of the Magnitude of a Radar Echo

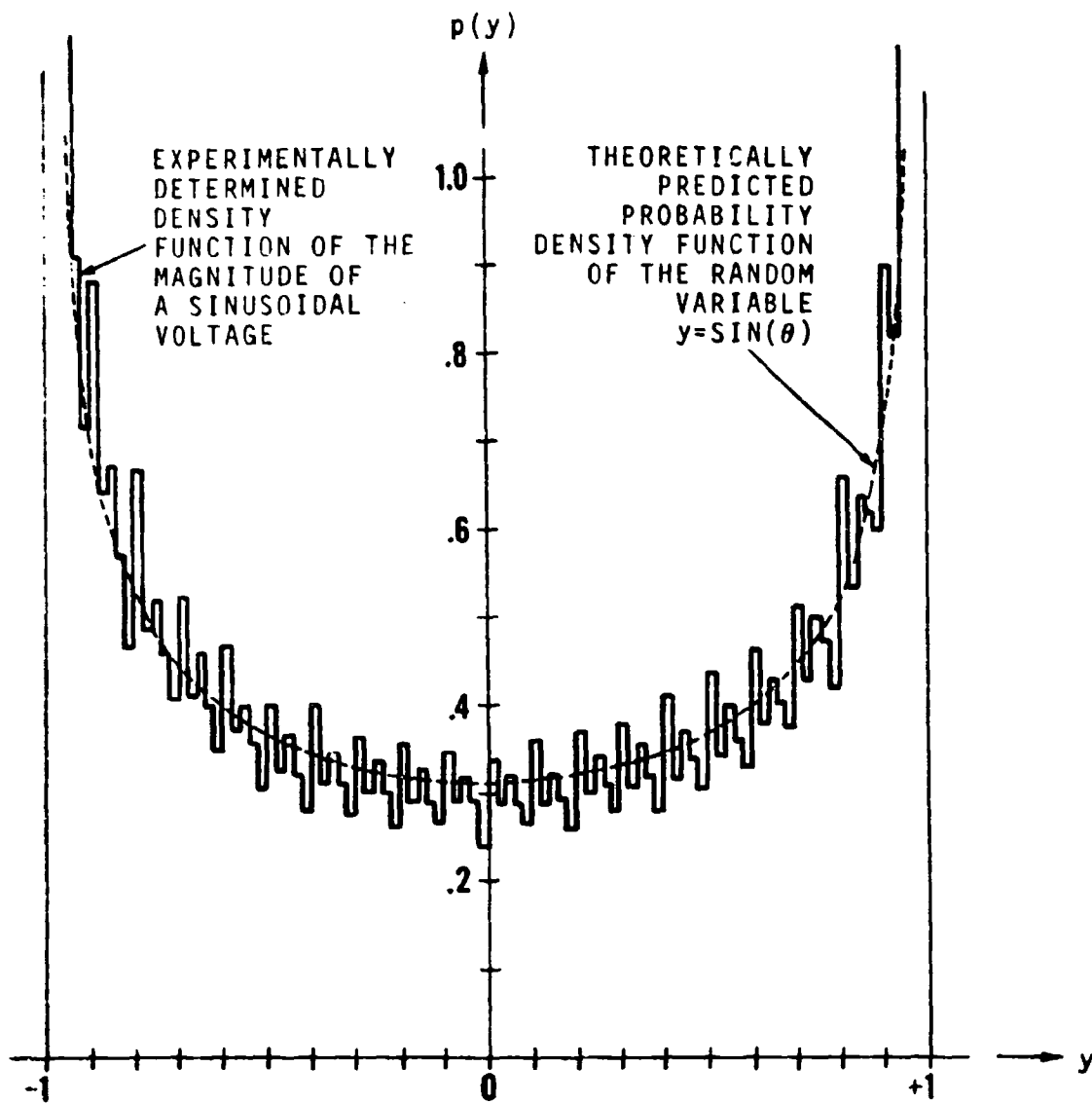


Figure 48. Results of a Test Run in Which a Sinusoidal Input was Sampled by the System of Figure 1

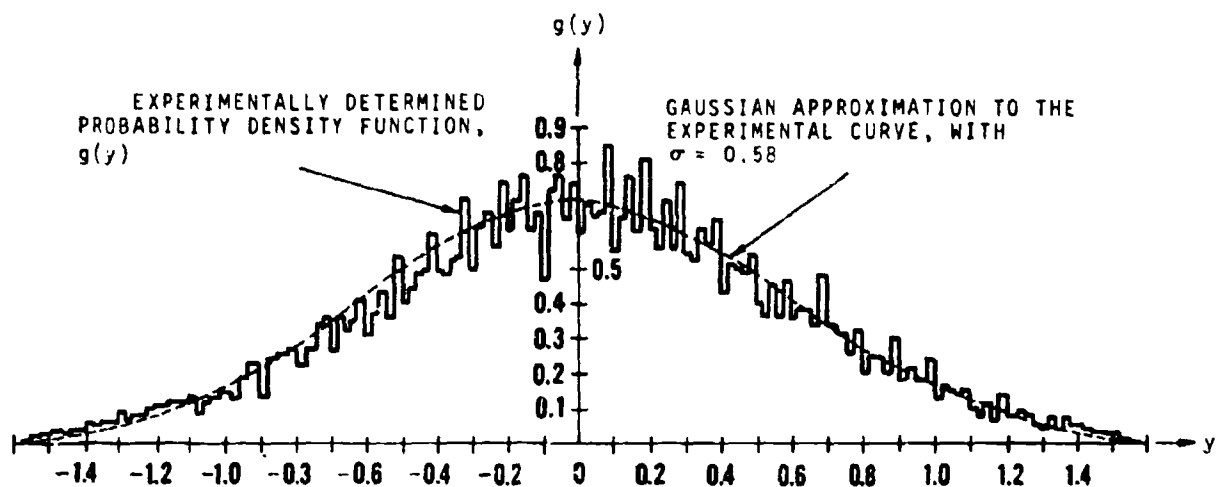


Figure 49. Probability Density Function of Radar Echo from a Line of Trees Beginning at 560 Yards Range with 0-3 mph Wind Velocity (Ref. ECOM - 01253-2, figure C-4)

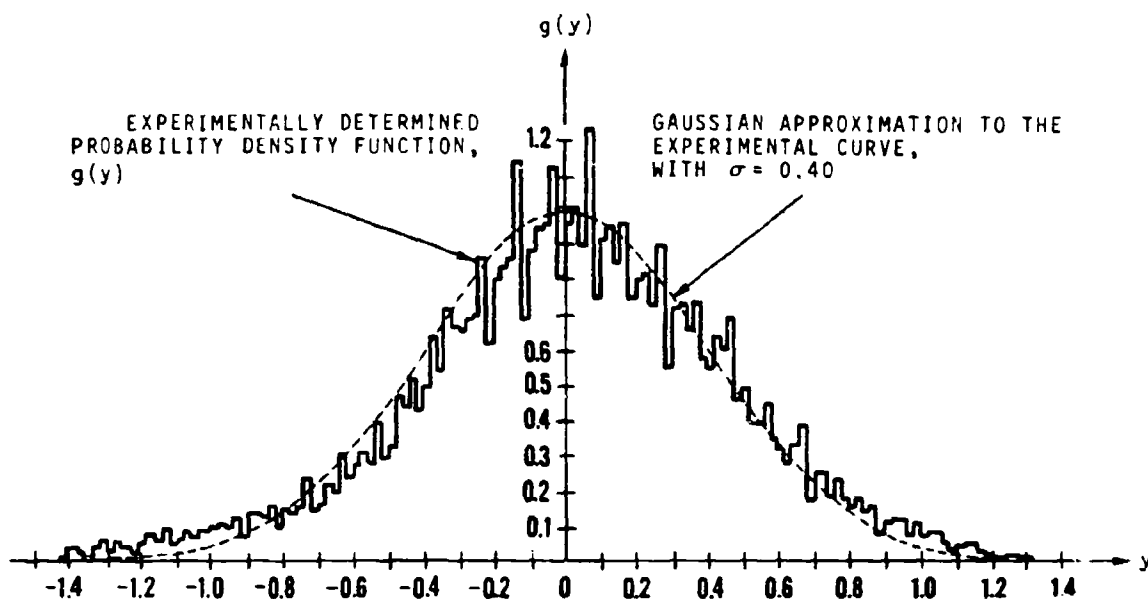


Figure 50. Probability Density Function of Radar Echo from a Line of Trees Beginning at 560 Yards Range with 10-14 mph Wind Velocity (Ref. ECOM - 01253-2, figure C-5)

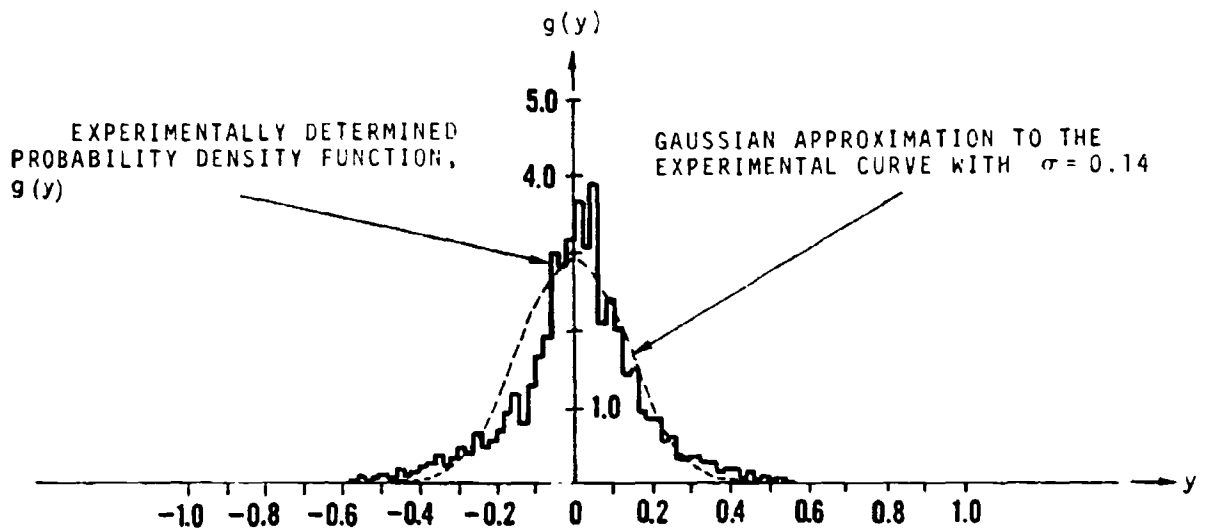


Figure 51. Probability Density Function of Radar Echo from Reference Sphere  
 (Ref. ECOM-01253-2, figure C-6)

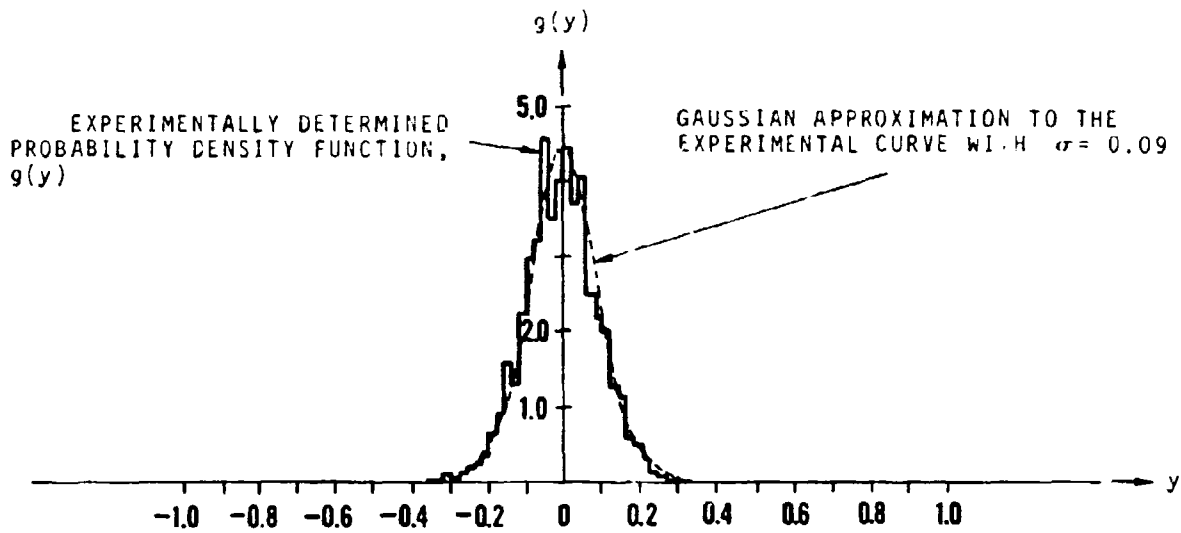


Figure 52. Probability Density Function of Radar Echo from Isolated Telephone Pole (Ref. ECOM - 01253-2, figure C-8)

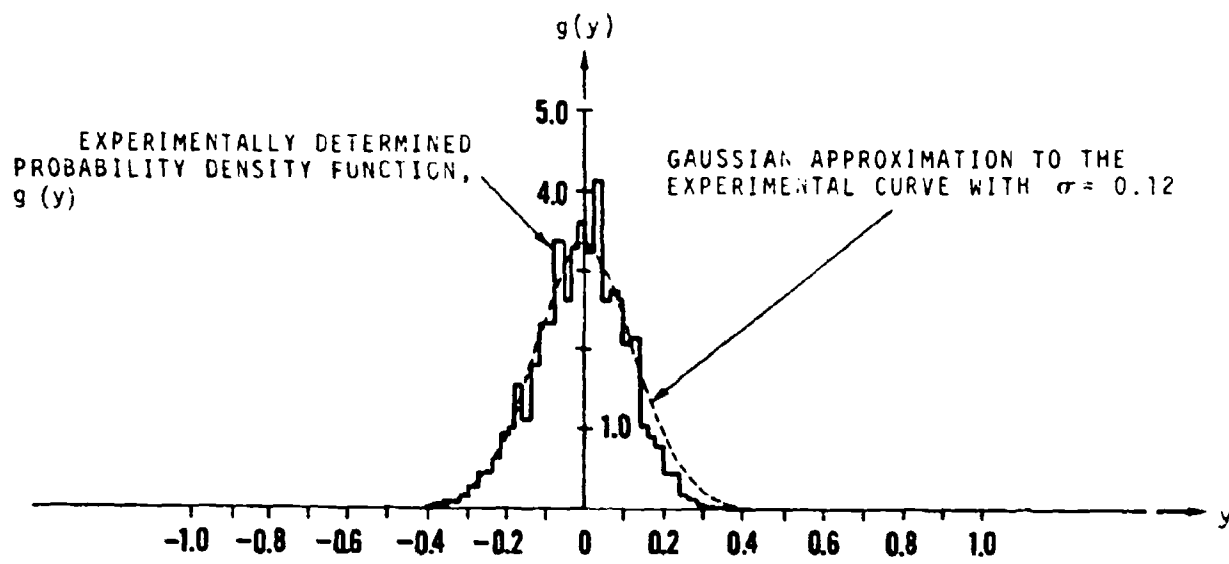


Figure 53. Probability Density Function of Radar Echo from Vertically Suspended Cable (Ref. ECOM - 01253-2, figure C-7)

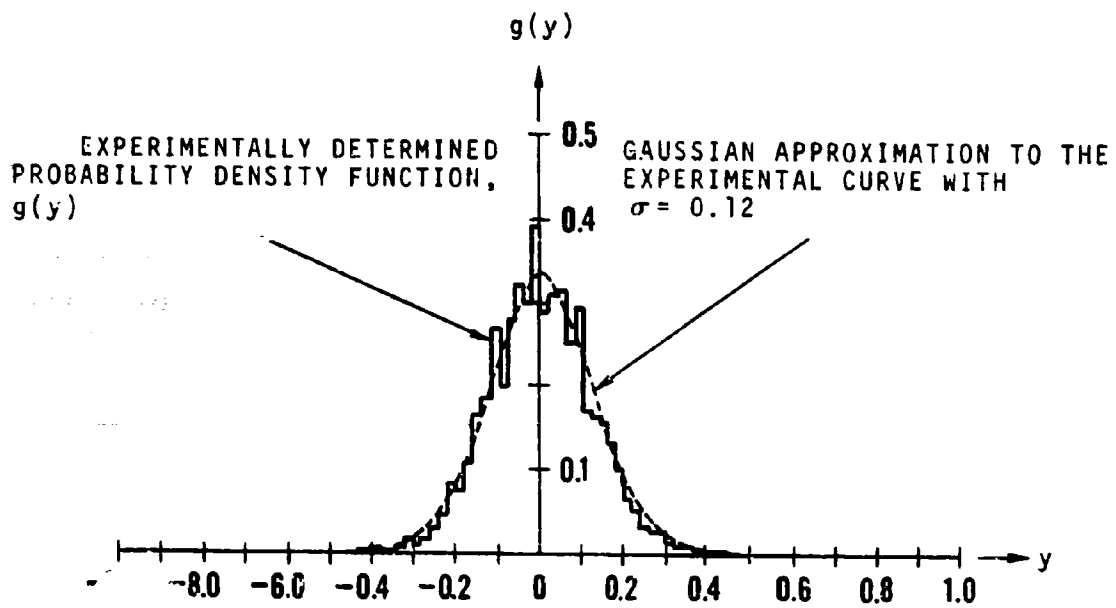


Figure 54. Probability Density Function of Radar Echo from Telephone Pole Viewed Against a Background of Trees Beginning at 560 Yards (Ref. ECOM-0-1253-2, figure C-12)

properly represent probability density functions, this area has been normalized to unity. In each case, a Gaussian probability density function

$$g_2(y) = \frac{1}{\sigma\sqrt{2\pi}} \exp \left[ -\frac{1}{2} \left( \frac{y-m}{\sigma} \right)^2 \right] \quad (29)$$

has been drawn on the same set of axes as the experimentally determined density function,  $g_1(y)$ . The Gaussian density is completely specified by specifying its mean,  $m$ , and standard deviation,  $\sigma$ . The mean of the Gaussian process was set equal to the computer calculated value of the sample mean of the video signal. In presenting the data the sample mean was set equal to zero, in each case. The standard deviation was chosen in such a way that the area under the experimental curve from  $(m - \sigma)$  to  $(m + \sigma)$  is equal to the area under  $g_2(y)$  over the same range.

#### 1.4.3.4 Conclusion

Based on Figures 49 through 54 several tentative conclusions can be made concerning the relationships between the nature of the radar target and the probability density function of its boxcarred, radar-video return. These are presented as follows:

- a. Each of the experimentally determined probability density functions can be well approximated by a normal distribution with a standard deviation selected as indicated in section 1.4.3.3. This result provides additional justification for our use of a normal approximation in the ground clutter simulator discussed in Appendix G of Technical Report ECOM-01253-2.
- b. A certain asymmetry about the sample mean can be observed to exist for each of the experimentally derived density functions. The asymmetry is more pronounced for clutter targets than for composite targets and for composite targets more than it is for isolated, stationary targets, with the exception of the reference sphere. Theoretical calculations based on a random scatter model [1] indicate the existence of such a trend. For low fixed-to-fluctuating target ratios, as in the case of clutter targets, the predicted distribution is an asymmetric Rayleigh distribution. Whereas, for high fixed-to-fluctuating target ratios, as in the case of isolated stationary targets, the predicted distribution is a symmetric Gaussian distribution. Hence, the increase in the symmetry of the density function as the fixed-to-fluctuating target ration increases.

- c. Figure 49 is the probability density function of the return from a patch of trees moving in a 0-3 mph wind. Figure 50 is the probability density function of the same patch of trees moving in a 10-14 mph wind. The standard deviation of the Gaussian density of Figure 49 was found to be equal to 0.58. Whereas, the standard deviation of the Gaussian density of Figure 50 was found to be equal to 0.40. Based on these two densities, it would appear that the higher the wind velocity, the narrower the probability density function.

This result is difficult to explain on the basis of a random scatterer model. In such a model, it is assumed that the radar echo is the vector sum of the radar returns from each individual scatterer. If it is assumed that the magnitude of the radar return from each individual scatterer is an independent random variable, obeying a particular density law, then the probability density function of the overall return is a complex function of the magnitudes of the individual returns and the density functions which they obey.

- d. Figure 54 is the probability density function of a composite target consisting of the patch of trees of Figure 49 and the telephone pole of Figure 52. The inclusion of a stationary target in the illuminated patch of clutter is seen to increase the probability of obtaining a sample of the video return whose magnitude lies in the neighborhood of the mean.

It is important to note that the statements enumerated above are made on the basis of the limited number of pieces of experimental data presented here. The tentative conclusions presented can, however, serve to indicate areas of investigation for a series of experiments presently being conducted by means of the radar system described in section 1.4.1 of this report.

## 2.

LITERATURE CITED

- [1] Kerr, D., "Propagation of Short Radio Waves," MIT Radiation Laboratory Series, volume 13, McGraw-Hill Book Company, Inc., New York, 1951, pages 550-587.
- [2] Goldstein, H., "The Effect of Clutter Fluctuations on MTI," MIT Radiation Laboratory Report 700, December 27, 1945.
- [3] Lord Rayleigh, "Theory of Sound," second edition, Volume 1, Macmillan, London, 1894, page 35.
- [4] Kerr, page 553.
- [5] Ibid., page 555.
- [6] Schwartz, M., "Information Transmission, Modulation, and Noise," McGraw-Hill Book Company, Inc., New York, 1959, chapter 7.
- [7] Barlow, E.J., "Doppler Radar," Proc. IRE, volume 37, April, 1949, pages 340-355.
- [8] Kerr, pages 571-587.
- [9] Urkowitz, H., et al, "Generalized Resolution in Radar Systems," Proc. IRE, volume 50, October, 1962, page 2093.
- [10] Rihaczek, A.W., "Radar Resolution Properties of Pulse Trains," Proc. IEEE, volume 52, February, 1964, page 153.
- [11] McCarthy, S.G., and Roth, I., "Electro-Optical Information Processing in the Space Domain," Sperry Engineering Review, volume 17, No. 1, Summer 1964, pages 22-30.
- [12] Silver, S., "Microwave Antenna Theory and Design", MIT Radiation Laboratory Series, Volume 12, McGraw-Hill Book Company, Inc., New York, chapter 6.
- [13] Lee, Y.W., "Statistical Theory of Communication," John Wiley and Sons, Inc., New York, 1960, pages 196-198.



14. KEY WORDS	LINK A		LINK B		LINK C	
	ROLE	WT	ROLE	WT	ROLE	WT
Radar		2				
Airborne		1				
Study		1				
Millimeter Radar		4				
Sensor		1				
Laser Radar		2				
Obstacle Detection		2				
Obstacle Analysis		1				
Antenna		1				
Backscatter		1				
70 GHz Radar		2				
Obstacle Avoidance		3				

INSTRUCTIONS

1. **ORIGINATING ACTIVITY:** Enter the name and address of the contractor, subcontractor, grantee, Department of Defense activity or other organization (*corporate author*) issuing the report.

2a. **REPORT SECURITY CLASSIFICATION:** Enter the overall security classification of the report. Indicate whether "Restricted Data" is included. Marking is to be in accordance with appropriate security regulations.

2b. **GROUP:** Automatic downgrading is specified in DoD Directive 5200.10 and Armed Forces Industrial Manual. Enter the group number. Also, when applicable, show that optional markings have been used for Group 3 and Group 4 as authorized.

3. **REPORT TITLE:** Enter the complete report title in all capital letters. Titles in all cases should be unclassified. If a meaningful title cannot be selected without classification, show title classification in all capitals in parenthesis immediately following the title.

4. **DESCRIPTIVE NOTES:** If appropriate, enter the type of report, e.g., interim, progress, summary, annual, or final. Give the inclusive dates when a specific reporting period is covered.

5. **AUTHOR(S):** Enter the name(s) of author(s) as shown on or in the report. Enter last name, first name, middle initial. If military, show rank and branch of service. The name of the principal author is an absolute minimum requirement.

6. **REPORT DATE:** Enter the date of the report as day, month, year, or month, year. If more than one date appears on the report, use date of publication.

7a. **TOTAL NUMBER OF PAGES:** The total page count should follow normal pagination procedures, i.e., enter the number of pages containing information.

7b. **NUMBER OF REFERENCES:** Enter the total number of references cited in the report.

8a. **CONTRACT OR GRANT NUMBER:** If appropriate, enter the applicable number of the contract or grant under which the report was written.

8b, 8c, & 8d. **PROJECT NUMBER:** Enter the appropriate military department identification, such as project number, subproject number, system numbers, task number, etc.

9a. **ORIGINATOR'S REPORT NUMBER(S):** Enter the official report number by which the document will be identified and controlled by the originating activity. This number must be unique to this report.

9b. **OTHER REPORT NUMBER(S):** If the report has been assigned any other report numbers (*either by the originator or by the sponsor*), also enter this number(s).

10. **AVAILABILITY/LIMITATION NOTICES:** Enter any limitations on further dissemination of the report, other than those imposed by security classification, using standard statements such as:

- (1) "Qualified requesters may obtain copies of this report from DDC."
- (2) "Foreign announcement and dissemination of this report by DDC is not authorized."
- (3) "U. S. Government agencies may obtain copies of this report directly from DDC. Other qualified DDC users shall request through \_\_\_\_\_."
- (4) "U. S. military agencies may obtain copies of this report directly from DDC. Other qualified users shall request through \_\_\_\_\_."
- (5) "All distribution of this report is controlled. Qualified DDC users shall request through \_\_\_\_\_."

If the report has been furnished to the Office of Technical Services, Department of Commerce, for sale to the public, indicate this fact and enter the price, if known.

11. **SUPPLEMENTARY NOTES:** Use for additional explanatory notes.

12. **SPONSORING MILITARY ACTIVITY:** Enter the name of the departmental project office or laboratory sponsoring (*paying for*) the research and development. Include address.

13. **ABSTRACT:** Enter an abstract giving a brief and factual summary of the document indicative of the report, even though it may also appear elsewhere in the body of the technical report. If additional space is required, a continuation sheet shall be attached.

It is highly desirable that the abstract of classified reports be unclassified. Each paragraph of the abstract shall end with an indication of the military security classification of the information in the paragraph, represented as (TS), (S), (C), or (U).

There is no limitation on the length of the abstract. However, the suggested length is from 150 to 225 words.

14. **KEY WORDS:** Key words are technically meaningful terms or short phrases that characterize a report and may be used as index entries for cataloging the report. Key words must be selected so that no security classification is required. Identifiers, such as equipment model designation, trade name, military project code name, geographic location, may be used as key words but will be followed by an indication of technical context. The assignment of links, rules, and weights is optional.